Fuel 429 (2027) 140731

Contents lists available at ScienceDirect

Fuel

journal homepage: www.elsevier.com/locate/fuel

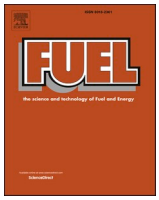

Full Length Article

Characterization and CO_2 gasification kinetics at high pressure of cenospheres from entrained flow gasification

Stella Walker [a,b,*], Manuel Nather [b], Angela Ullrich [b], Zahra Ghasemi Monfared [c], Kentaro Umeki [c], Thomas Kolb [a,b]

[a] Karlsruhe Institute of Technology, Engler-Bunte-Institute, Fuel Technology, EBI ceb, Engler-Bunte-Ring 1, 76131 Karlsruhe, Germany
[b] Karlsruhe Institute of Technology, Institute for Technical Chemistry, ITC vgt, Hermann-von-Helmholtz-Platz 1, 76344 Eggenstein-Leopoldshafen, Germany
[c] Luleå University of Technology, Department of Engineering Sciences and Mathematics, Division of Energy Science, 97187 Luleå, Sweden

ARTICLE INFO

Keywords:
Cenosphere
Biogenic pyrolysis oil
Slurry
Entrained flow gasifier
Pressurized gasification kinetics

ABSTRACT

Cenospheres are plausible intermediates in entrained flow gasification (EFG) of biogenic suspension fuels. However, their structure and reactivity remain poorly understood, limiting the accuracy of numerical simulations of entrained flow gasifiers.

The present study characterizes cenospheres from two experiments in a technical entrained flow gasifier using beech wood pyrolysis oil (PO) and char suspensions (slurry; POC) under intentionally low air ratios (0.35). Structural features and CO_2 gasification kinetics are investigated, and mass transport effects under technically relevant conditions (1000 – 1500 °C, 10 bar CO_2) are evaluated.

A broad particle size distribution of the cenospheres (100 – 800 μm) is identified. Micro computer tomography reveals internal macro-structures ranging from uniformly distributed porosity to a porous shell, with embedded char particles in POC cenospheres.

Micro- and mesoporosity are analyzed via argon physisorption. Only POC cenospheres show microporosity, which is assigned to the char particles. Structural ordering determined by X-ray diffraction (XRD) is stronger for smaller cenospheres. The evolution with increasing particle diameter differs between POC and PO cenospheres, with radial expansion of the graphene layers prevailing in POC cenospheres, while both radial expansion and graphene stacking vary in the structured domains in PO cenospheres.

Reaction kinetics in CO_2 (5 – 20 bar, 810 – 850 °C) are determined in the differential fixed bed reactor for 200 – 400 and 600 – 800 μm fractions. The reaction rate increases with increasing temperature and CO_2 partial pressure as described by the Arrhenius and the power law model (activation energy: 210 – 242 kJ/mol; reaction order: 0.2 – 0.3). Especially the mantle area-to-volume ratio of the stacked graphene layers derived from XRD and the mesopore surface area are found to impact the reaction rate.

1. Introduction

Cenospheres are porous, hollow spheres known from combustion of coal (ash cenospheres: [1], carbon cenospheres: [2]) and biomass particles (carbon cenospheres: [3]), heavy fuel oil (HFO) [4–10] or biogenic pyrolysis oil (PO) droplets [11–13]. In the case of liquid fuels, the formation process has been studied mainly for HFO [4,7–10], but also for PO [11–13], typically at atmospheric pressure and in air or nitrogen atmosphere. For example, cenosphere formation was observed during drop-tube experiments with straw oil and beech wood oil droplets at 1200 °C [13] and during experiments with pine oil and oak oil droplets released into a flat-flame burner at 1327 °C [11].

Generally, the following stages of cenosphere formation from PO are distinguished:

First, water and lower boiling components evaporate. In this stage, mass transport from the droplet volume to the outer surface is fast. Calabria et al. [12] observed this stage at temperatures up to 130 °C and at atmospheric pressure for a suspended droplet of forestry residue PO.

Second, with further increasing temperature, especially the outer regions of the droplet accumulate higher boiling components and therefore develop higher viscosity. Oxygen-containing organic species are prone to polymerize. Heavier components crack above 300 – 350 °C,

* Corresponding author at: Engler-Bunte-Ring, 176131, Karlsruhe, Germany.
E-mail address: stella.walker@kit.edu (S. Walker).

https://doi.org/10.1016/j.fuel.2026.140731
Received 12 May 2026; Received in revised form 24 June 2026; Accepted 17 July 2026

which contributes to a further increase in viscosity and the creation of a viscous shell. This in turn strongly affects mass transport of volatiles to the droplet surface. Released volatiles can splash out by so-called micro-explosions.

Third, due to the low permeability of the outer shell, volatiles of higher boiling components are trapped inside the droplet and internal pressure increases. In the case of low heating rates, the droplet swells slowly.

Calabria et al. found strong swelling and bubbling of suspended forestry residue PO droplets in the temperature range of 130 – 500 °C [12]. For high heating rates (e.g. in the vicinity of a flame), the shell expands, distorts and pressure is released through blowholes [4,7].

Finally, the shell coalesces and the matrix further pyrolyzes to char [4,7,12,13].

In contrast to combustion processes, the possibility of cenosphere formation and conversion during entrained flow gasification (EFG) of biogenic PO or suspensions of PO and char particles (POC) has not been considered in depth in literature to the best of our knowledge. However, in principle, formation of cenospheres from PO or POC droplets in the entrained flow reactor is to be expected:

Entrained flow gasifiers are operated at high temperatures (typically > 1200 °C) and often at high pressures and allow for conversion of liquid or suspension fuels to synthesis gas [14,15]. During gasification of PO or POC with steam and oxygen in the bioliq gasifier at Karlsruhe Institute of Technology (KIT), the fuel is atomized into the reactor to create droplets with a high specific surface area for the following conversion steps. Based on the instantaneous and time-averaged flow and temperature fields as well as particle trajectories resulting from CFD simulations, the temperature and reaction zones traversed by the droplets can be defined [16–19]. Close to the burner in the so-called core zone, the jet of dispersed droplets and gas phase (H_2O and O_2) expands radially at a high velocity. The medium is heated up from the low inlet temperature to approximately 1200 °C (1500 K). Due to the high momentum of the incoming gas stream and the confinement of the reactor chamber walls, syngas is re-entrained into the oxygen-rich turbulent jet. In this hot oxidation zone ($T_{gas} > 1800$ °C (2100 K)), oxygen is consumed by the re-entrained synthesis gas and by volatiles released from the fuel droplets that undergo fast heat-up.

From this description of EFG, it can be deduced that entering droplets undergo fast heat-up with especially high heating rates ($dT/dt \approx 10^4 - 10^5$ K/s) and high temperatures, which can lead to cenosphere formation.

With increasing distance from the burner, the jet cross-section increases and the velocity further decreases. The gas temperature decreases because of oxygen depletion and abatement of the exothermal and prevalence of endothermal reactions. In the presence of H_2O and CO_2, carbon-rich particles, potentially cenospheres, undergo heterogeneous gasification reactions (equations (1) and (2)), producing synthesis gas. This zone is referred to as gasification zone. The synthesis gas stream either leaves the reactor chamber towards the dip water quench or recirculates [16–19].

$$C + H_2O \rightarrow CO + H_2 \quad (1)$$

$$C + CO_2 \rightarrow 2\,CO \quad (2)$$

So far, research on these reactions in the context of EFG of biogenic fuels focused on gasification of char particles [20–26]. The potential formation of cenospheres as intermediates during EFG of PO or POC may however significantly affect assumptions for numerical simulation regarding solid conversion in heterogeneous gasification reactions. For example, the gasification kinetics may be affected by different micro-kinetics and micro-sale diffusion lengths. This in turn may severely affect the performance of the gasifier, especially the efficiency and carbon conversion, two key challenges in research on biomass gasification [27]. To date, no studies addressing the gasification kinetics of cenospheres from POC and PO at EFG conditions have been reported.

This publication aims to tackle this underexplored area. The understanding of the time–temperature-history of the droplets within the entrained flow reactor, combined with current knowledge on cenosphere formation and with successful cenosphere formation in drop-tube experiments with POC and PO [13], provided the motivation to conduct experiments in the pressurized pilot reactor aimed at recovering cenospheres potentially formed as intermediates during EFG.

Two experiments at the bioliq entrained flow gasifier were conducted at a total pressure of 40 bar, one with a suspension of beech wood PO with 10 wt-% char particles (POC) and one with beech wood PO. Low stoichiometric ratios of 0.35 resulted in lower temperatures and incomplete fuel conversion. It was postulated that the processes of cenosphere formation and conversion would be slower at lower temperatures, increasing the possibility that the producer gas leaving the reactor chamber could entrain unreacted cenospheres into the dip water quench (see supplementary material H). The solids found in the dip water quench after the experiments were characterized and their CO_2 gasification kinetics up to CO_2 partial pressures of 20 bar were investigated.

While the results of this study suggest that cenospheres may form as intermediates during EFG, it should already be noted that the currently available evidence does not yet allow this to be confirmed conclusively.

2. Materials and methods

A characterization of the beech wood char particles and the beech wood pyrolysis oil used as a feed for the gasification experiments can be taken from the supplementary material A.

The particles found in the dip water quench were suspended in demineralized water and then carefully dried at 105 °C (as indicated in DIN EN ISO 18134) and sieved to size fractions of 100 – 200 µm, 200 – 400 µm, 400 – 600 µm, 600 – 800 µm, and 800 – 1000 µm. The samples are denoted according to the size fractions, as exemplarily shown in Table 1. The samples used for the analyses described below were carefully taken from the respective sample containers with the aim of capturing the overall particle population as well as possible.

2.1. Chemical analyses

The sieved samples were subjected to proximate and ultimate analysis (DIN EN ISO 16948: C, H, N, S (O by difference); DIN 51719: ash; DIN 51720: volatile matter; DIN 51718: moisture; fixed carbon is calculated by difference). The analyses were done by DVGW Research Center at Engler-Bunte-Institut (DVGW EBI, KIT). To ensure reproducibility, analyses were repeated four times.

2.2. Scanning electron microscopy and scanning electron microscopy coupled with energy dispersive X-ray spectroscopy

Scanning electron microscopy (SEM) was conducted at the Laboratory for Electron Microscopy (LEM, KIT; scanning electron microscope LEO 1530, LEO (formerly Zeiss)) for receiving a magnification of the obtained samples.

The samples were also subjected to scanning electron microscopy coupled with energy dispersive X-ray spectroscopy (EDXS) for determination of elemental composition (LEM, KIT; SEM: QUANTA FEG 650, FEI; EDXS: QUANTAX 400, Esprit 1.9, Bruker).

Table 1
Particle size fractions and notation.

Particle size fraction	Notation for samples obtained from experiment…	
	POC	PO
200 – 400 µm	POC_200-400	PO_200-400
400 – 600 µm	POC_400-600	PO_400-600
600 – 800 µm	POC_600-800	PO_600-800

2.3. Particle size analysis

Particle size analysis was carried out by 3P instruments with a Bettersizer S3 Plus. The samples were dispersed in water. 1,000,000 particles were analyzed with laser diffraction and dynamic image analysis and the area-equivalent diameter was received.

2.4. Analysis of the internal structure and the pore size distribution

2.4.1. Argon physisorption

Argon physisorption was used to determine the specific surface area and the pore size distribution of approximately 0.7 – 50 nm of the sample fractions and the beech wood char used in the EFG experiment with POC. Analyses and data evaluation were carried out by 3P instruments using a 3P micro300 (3P instruments). The samples ($0.13\,g \leq m_{sample} \leq 0.29\,g$) were outgassed at 120 °C for 7 h before analysis. The adsorption isotherms were measured at 87 K in a range of $0 < p/p_{sat} \leq 0.95820 - 0.97641$ of relative pressure (related to the saturation vapor pressure p_{sat}). The total pore volume was determined based on Gurvich method (following DIN 66134). To characterize the micro- and mesopores, the adsorption branch of the isotherms was analyzed following the Quenched Solid Density Functional Theory (QSDFT).

The reproducibility of the physisorption experiments was verified by means of sample POC_200-400. Three physisorption isotherms were recorded for three samples of this fraction.

2.4.2. Micro computer tomography

X-ray micro computer tomography (μCT) enables the visualization of the internal structure of solids and the quantification of the pore structures in the micrometer scale. The samples analyzed with μCT are subjected to X-ray transmission from 360 °. The numerical reconstruction of the 3-dimensional structure is based on the attenuation of the X-rays that passed through the object in all spatial directions.

μCT scans of the cenospheres were conducted at Luleå University of Technology (LTU) with an X-ray micro tomograph Xradia 510 Versa (Zeiss). An acceleration voltage of 40 kV and X-ray tube power of 3 W were set. Either 1601 or 3201 projections were acquired over a full 360 ° rotation of the sample. Up to a particle diameter of 400 μm, a cylindrical sample holder with a height of 1 mm and a diameter of 1 mm was used. Larger particles were analyzed in a sample holder with a height of 2 mm and a diameter of 2 mm. The achieved resolution was 1 μm.

The reconstruction and further evaluation of the raw data was done with the software Dragonfly (Version 2022.2) [28]. With Open Pore Network Model (OpenPNM) implemented in Dragonfly, the pores were analyzed. In OpenPNM, the pore network is structured such that each throat connects exactly two pores. One pore in turn can have many throats. A detailed description of the pore network modeling package can be found in [29].

The workflow is summarized in Fig. 1. Prior to conducting the pore analysis, the pore space had to be defined. First, a sphere containing one particle was selected and segmented (A). Second, the voxels of the voids in the pores were selected in two steps. Using the “Region of Interest” (ROI) Tool in Dragonfly, a voxel intensity range of the voids is defined and selected, thus creating a binary image which separates solid and void. The selection was then further refined with implemented functions (“Fill inner 3D Area” and “Process Islands”) (B). Third, the region surrounding the particle (indicated by blue arrows in (B)) was removed

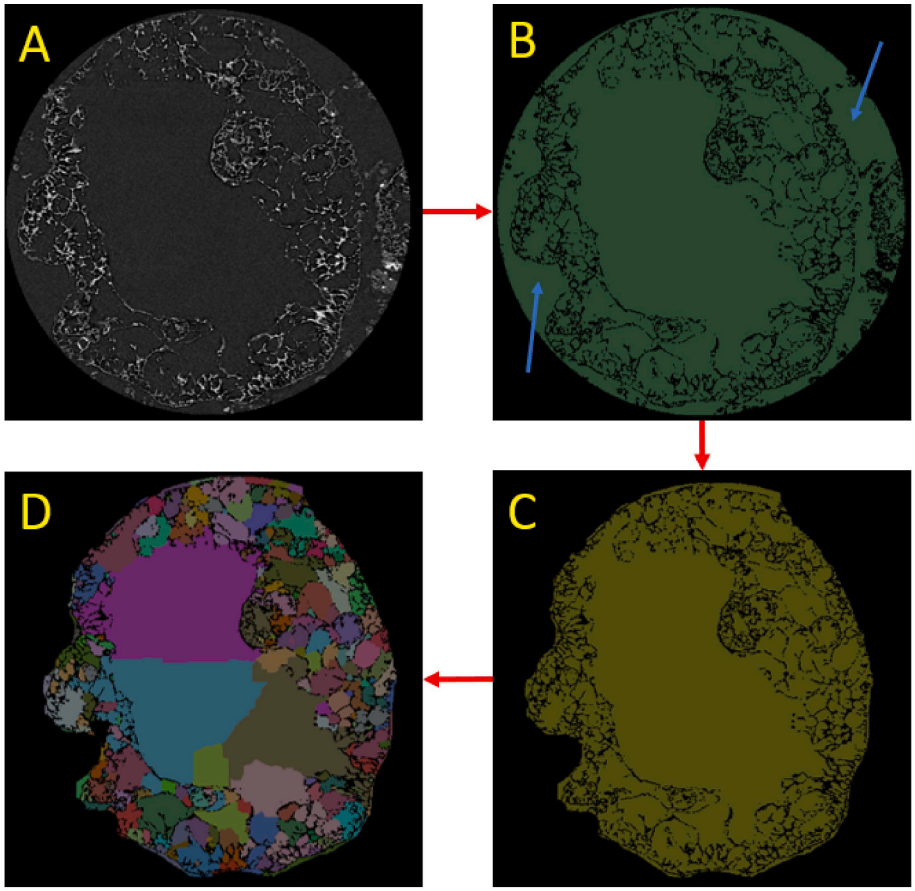

Fig. 1. Workflow of the pore analysis in Dragonfly: Selection of a particle (A), selection of the voxels of the voids (pores) (B), removal of the region surrounding the particle (C), OpenPNM analysis (D); red arrows indicate the workflow, blue arrows indicate the removed region surrounding the particle. (For interpretation of the references to colour in this figure legend, the reader is referred to the web version of this article.)

manually (C). The isolated pore space can then be analyzed using OpenPNM, which divides the void into pores (D, pore division is indicated by different colors (colors have no meaning)). From OpenPNM, different data on the pore network can be obtained, e.g., the equivalent diameter.

Owing to limited processing capacity, the resolution had to be adjusted to 2.2 μm. Consequently, macropores of an equivalent diameter below 2.2 μm could not be detected. This limitation is acknowledged in the present study.

As the workflow is time-consuming, three particles of POC_200-400, POC_600-800, PO_200-400 and PO_600-800 each were analyzed. To ensure representativeness, prior to the OpenPNM analyses, all imaged particles were thoroughly evaluated, and three particles per sample that were considered representative in terms of morphology and structural features were selected for subsequent pore network modelling. Despite careful selection, it should be emphasized that the quantitative OpenPNM analyses are not intended to support definitive conclusions. In this study, they were mainly employed for preliminary assessments of mass transport (section 4).

Verification of the pore size distribution resulting from OpenPNM analysis is rather difficult. The division into pores and throats happens in a three-dimensional model. Conversely the images (Fig. 1.) are only two-dimensional thus making it difficult to see the whole structure and comprehend the division into pores.

2.4.3. Skeletal density

The skeletal density of a particle is defined as the particle mass in relation to the solid volume (without pore volume). It was determined with a helium pycnometer (Micro Ultrapyc 1200e, Quantachrome Instruments) at 20 °C. About 500 – 1500 mg of sample (depending on the particle size) was used for one run and each measurement was repeated twice.

2.4.4. Estimation of the total porosity

From the gasification experiments in the differential fixed bed reactor (dFBR, see section 2.6.), a mass-specific reaction rate is derived. However, for the assessment of the influence of mass transport during the gasification experiments (through the Weisz-Prater criterion, section 3.5.) and during EFG, the volumetric reaction rate r_V is needed. Calculation of the volumetric reaction rate requires the particle density, thus the total porosity.

Mercury intrusion represents the most straightforward method for porosity determination and pore size analysis from nanometer to micrometer scale, but it comes with some limitations. First, during preliminary tests, the high pressure necessary for mercury intrusion into narrow pores destroyed thin-walled pore structures of the investigated particles, a problem also reported in [30]. Second, the size of large cavities in the particles are in the same order of magnitude as the size of interparticle voids in the packing, which made distinguishing between both impossible. Therefore, the skeletal density $\rho_{skeletal}$ (in g/mm^3) and mass-specific micro- and mesopore volume $V_{micro-meso}$ (in mm^3/g determined by argon physisorption) were combined with the particle diameter and the macropore size distribution (for macropores larger than 2.2 μm) obtained from OpenPNM analyses of the μCT scans. A similar approach, combining bulk methods and single-particle optical pore analysis, was recently also employed for walnut shell char by Freisewinkel et al. [30].

The volume of the macropores $\ddot{V}_{macro}$ (larger than 2.2 μm) of one single particle is approximated from the macropore pore size distribution of d_{pore} (in mm) obtained from μCT analyses and OpenPNM results assuming spherical pores (equations (3) and (4)).

$$\ddot{V}_{pore,i} = \frac{4}{3}\cdot\pi\cdot\left(\frac{d_{pore,i}}{2}\right)^3 \quad (3)$$

$$\ddot{V}_{macro} = \sum\nolimits_i \ddot{V}_{pore,i} \quad (4)$$

The particle volume of the same particle $\ddot{V}_{particle}$ is estimated with the particle diameter $d_{particle}$ (in mm) obtained from Dragonfly [28] (eq. (5)).

$$\ddot{V}_{particle} = \frac{4}{3}\cdot\pi\cdot\left(\frac{d_{particle}}{2}\right)^3 \quad (5)$$

To include the specific volume of the micro- and mesopores $V_{micro-meso}$ (in mm^3/g) in the porosity calculation, the following set of equations (6) to (8) is iteratively solved and the mass and the total porosity of the analyzed particle are obtained:

$$m_{particle,j} = (1-\varepsilon_{tot,j})\cdot\ddot{V}_{particle}\cdot\rho_{skeletal} \quad (6)$$

$$\ddot{V}_{micro-meso,\,j} = V_{micro-meso}\cdot m_{particle,j} \quad (7)$$

$$\varepsilon_{tot,j} = \frac{\ddot{V}_{macro} + \ddot{V}_{micro-meso,j}}{V_{particle}} \quad (8)$$

(Volumes $\ddot{V}$ in (mm^3) relate to the particle examined.)

2.5. Analysis of the carbon structure

Gasification reactivity is strongly dependent on the degree of structural ordering of the carbon matrix (graphitization), i.e. the arrangement of graphene-like domains (in the following “graphene domains”) in stacking direction and within the basal plane [21,24,31,32]. X-ray diffraction (XRD) and Raman spectroscopy have been proven to be useful tools for the determination of stacking height and the width of graphene domains in carbon based materials [33–36].

The sample fractions were analyzed with XRD to gain information about the structure of the carbon matrix. The XRD results were validated against Raman spectroscopy. Confocal Raman analysis was performed using a WITec alpha300 R equipped with a 488 nm Laser operated at 2 mW. Further details on the method and results of the Raman spectroscopy can be taken from the supplementary material B.

The XRD analyses were performed using an Empyrean diffractometer (goniometer radius 240 mm, Malvern-PANalytical) equipped with a multistrip PIXcel^{3D} detector (255 channels, simultaneously covering 3.347° 2θ), CuKα-radiation (40 mA, 40 kV) and Bragg-Brentano optics. Measurements were conducted in the range of 5 to 120° 2θ with step size 0.013° 2θ, 98 s/step.

The samples were compacted in the sample holder for measurement.

The most inhomogeneous sample was chosen for estimation the maximum error originating from sample inhomogeneities (figure S.2 in supplementary material, B). Three different samples of POC_100-200 were measured and the standard deviation was calculated.

More details on the measurement method are given in the supplementary material B.

The (002) and (100) peaks of carbon at approximately 24° 2θ and 44° 2θ were refined for all samples to assess the degree of structural ordering (graphitization) of the carbon matrix as for example described in [21,37]. The reflection at 24° 2θ (attributed to the (002) peak) arises from the stacking of graphene layers. The second maximum at 44° 2θ (the (100) peak) originates from in-plane ordering of aromatic structures within these layers [36]. The coherence lengths L_a and L_c corresponding to the lateral in-plane coherence length (L_a, (100)) and the stacking coherence length perpendicular to the layers (L_c, (002)) of structured regions were determined by use of the fundamental parameters approach implemented in the TOPAS V7 software (Bruker-AXS). Hence, peak shapes and therewith sizes of the clusters were refined by application of physically based models that include also the instrumental parameters.

In addition, the interlayer spacing d_{Layers} was calculated according to Bragg equation (9):

$$2 \cdot d_{\text{Layers}} \cdot sin(\theta) = n \cdot \lambda \quad (9)$$

with $n = 1$ and $\lambda = 1.54056$ Å.

2.6. Gasification experiments in CO_2

Gasification experiments of POC_200-400, POC_600-800 as well as PO_200-400 and PO_600-800 were conducted at CO_2 partial pressures of 5 – 20 bar and at reaction temperatures of 810 – 850 °C in the dFBR developed at KIT [20,38,39]. In the gasification experiments, CO_2 partial pressures corresponded to the total pressures despite one experiment with PO_200-400 where the influence of total pressure on the CO_2 gasification kinetics was investigated.

Table 2 gives an overview over the conducted experiments. Each experiment was repeated at least three times with a sample mass of 25 ± 1 mg.

Since the dFBR and the experimental procedure are described in [20,38,39], the reader is referred to these publications for a detailed description.

The carbon conversion $X_{\text{C,gasif}}(t)$ is derived from the product gas concentrations and normalized to the gasified carbon mass (supplementary material section C) [20]. Conversions normalized to the fixed carbon mass introduced in the reactor ranged below 100 %. The corresponding values and a brief discussion can be found in the supplementary material C.

The reaction rate is derived by fitting the carbon conversion $X_{\text{C,gasif}}(t)$ to the Uniform Conversion Model (UCM; eq. (10)) for $0.05 \leq X_{\text{C,gasif}} \leq 0.8$ and following eq. (11) [38].

$$X_{\text{C,gasif}}(t) = 1 - \exp(-R_{\text{UCM}} \cdot t) \quad (10)$$

$$r = \frac{R_{\text{UCM}}}{\widetilde{M}_{\text{C}}} \quad (11)$$

The UCM assumes homogeneously distributed reactive centers over the whole particle volume. During conversion, the reactions take place at all reactive centers [21,40–42].

The pressure dependence of the reaction rates was modeled with a power law (PL) expression (eq. (12)). In eq. (12), the temperature dependence of the reaction rate is expressed in the rate constant k, while the pressure dependence is modeled with the reaction order n.

$$r = k(T_{\text{reaction}}) \cdot p_{\text{CO}_2}^{n} \quad (12)$$

The temperature dependence of k was described by the Arrhenius model (eq. (13)).

$$k(T_{\text{reaction}}) = k_0 \cdot \exp\left(-\frac{E_{\text{A}}}{\text{R}_{\text{U}} \cdot T_{\text{reaction}}}\right) \quad (13)$$

3. Results

3.1. Size fractions: SEM and chemical analyses

The particle size distributions (equivalent diameter, q3) of the samples resulting from the experiments with POC and PO are presented in Fig. 2. The distribution is defined by the quantiles $d_{10,\text{POC}} = 44.5$ µm and $d_{90,\text{POC}} = 733.5$ µm for the experiment with POC and by $d_{10,\text{PO}} = 49.1$ µm and $d_{90,\text{PO}} = 513.4$ µm for the experiment with PO.

Table 2
Experimental parameters for CO_2 gasification experiments.

Samples	POC_200-400, POC_600-800, PO_200-400, PO_600-800	PO_200-400
T_{reaction}/ °C	810, 830, 850	850
p_{tot}/ bar	5, 10, 20	20
p_{CO_2}/ bar	$= p_{\text{tot}}$	10

At this point, it is important to note that the particle size distribution determined ex situ may not fully reflect the actual distribution under reactor conditions.

Fig. 3 shows SEM images of the sieving fractions between 200 µm and 800 µm for both sample types (POC and PO experiments). The fractions of $d_{\text{Particle}} \geq 200$ µm consist of cenospheres of mostly spherical shape.

Table 3 summarizes the proximate analyses. Ash, volatiles, moisture and fixed carbon contents only marginally change with the particle size of POC, respectively PO cenospheres. Especially the moisture content of POC cenospheres after drying at 105 °C for at least 8 h is elevated. It is possible that moisture is trapped in the inner structure of the cenospheres (see section 3.2.).

The ash components found in the cenospheres originate not only from the ash inherent in the beech wood char and the pyrolysis oil, but also from the gasification process, such as slag from the cooling screen and glass used as model slag in preceding EFG experiments (see section 3.2.). Despite careful flushing of pipes and fittings of the bioliq entrained flow gasifier, some glass beads remained in the plant and were found in the samples (especially samples from the POC experiment, since this experiment was conducted first). Consequently, a meaningful interpretation of the ash composition was not feasible. The ash compositions are given in the supplementary material E.

Table 4 summarizes the elemental composition of the cenospheres ($d_{\text{Particle}} \geq 200$ µm) on a dry, ash-free basis. As for the proximate analyses (table 3), also the elemental composition of the cenospheres from one feed is roughly constant irrespective of the particle size. Cenospheres from POC reveal lower carbon and hydrogen but higher oxygen contents than samples of PO. SEM-EDXS measurements provided additional confirmation of this finding. While oxygen could be clearly identified as a component in the carbon matrix of the POC cenospheres, only trace amounts were found in the PO cenospheres (see supplementary material D).

This is remarkable as cenospheres from POC have lower volatile content compared to cenospheres from PO, which usually corresponds to higher (fixed) carbon and lower oxygen contents. The higher oxygen content of POC cenospheres is also noteworthy for another reason: the original char particles had lower oxygen content compared to the PO (8.6 wt-% vs. 30.6 wt-%), resulting in a lower oxygen content in the feed of the POC experiment than in the feed of the PO experiment (supplementary material A).

Comparison with available literature allows for a speculative discussion of possible factors influencing the carbon and oxygen contents of POC and PO cenospheres.

POC and PO cenospheres presented in this work reveal lower carbon content than Stoesser et al. found for cenospheres from atmospheric pyrolysis of wood and straw PO in a drop-tube reactor at 1200 °C in nitrogen with a residence time of 3 s, thus longer residence times compared to EFG (carbon contents: 97.4 – 97.6 %) [13]. In the samples presented in [13], hydrogen contents ranged from 1.7 to 1.9 %, thus comparable to PO cenospheres. Oxygen contents of 0.5 – 0.6 % are lower than the oxygen contents of POC and PO cenospheres. Hence, especially the reduction of the oxygen content may be part of the process of cenosphere formation from pyrolysis oil, most probably during polymerization and growth of graphene layers. Longer residence times may allow for a stronger reduction of the oxygen content.

Moreover, the higher oxygen content of POC cenospheres could potentially be related to the higher ash content. The ash contains Al, Ca, Fe, K, Mg, Na and Si, which may exist as oxides and carbonates, thus contain oxygen (see supplementary information E for ash analyses).

At this point, it is important to emphasize that both approaches cannot be quantitatively substantiated and require further investigation.

3.2. Morphology of the cenospheres

Fig. 4 (a) shows a cenosphere and a magnification of the surface of a

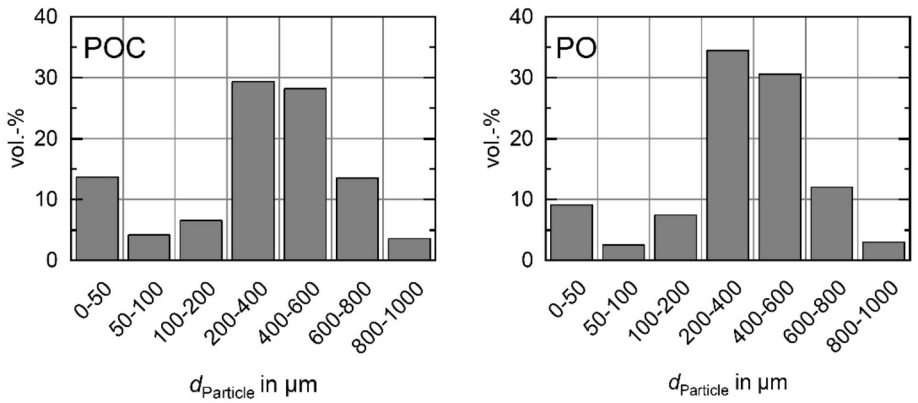

Fig. 2. Particle size distribution of the samples produced during EFG experiments with POC (left) and PO (right).

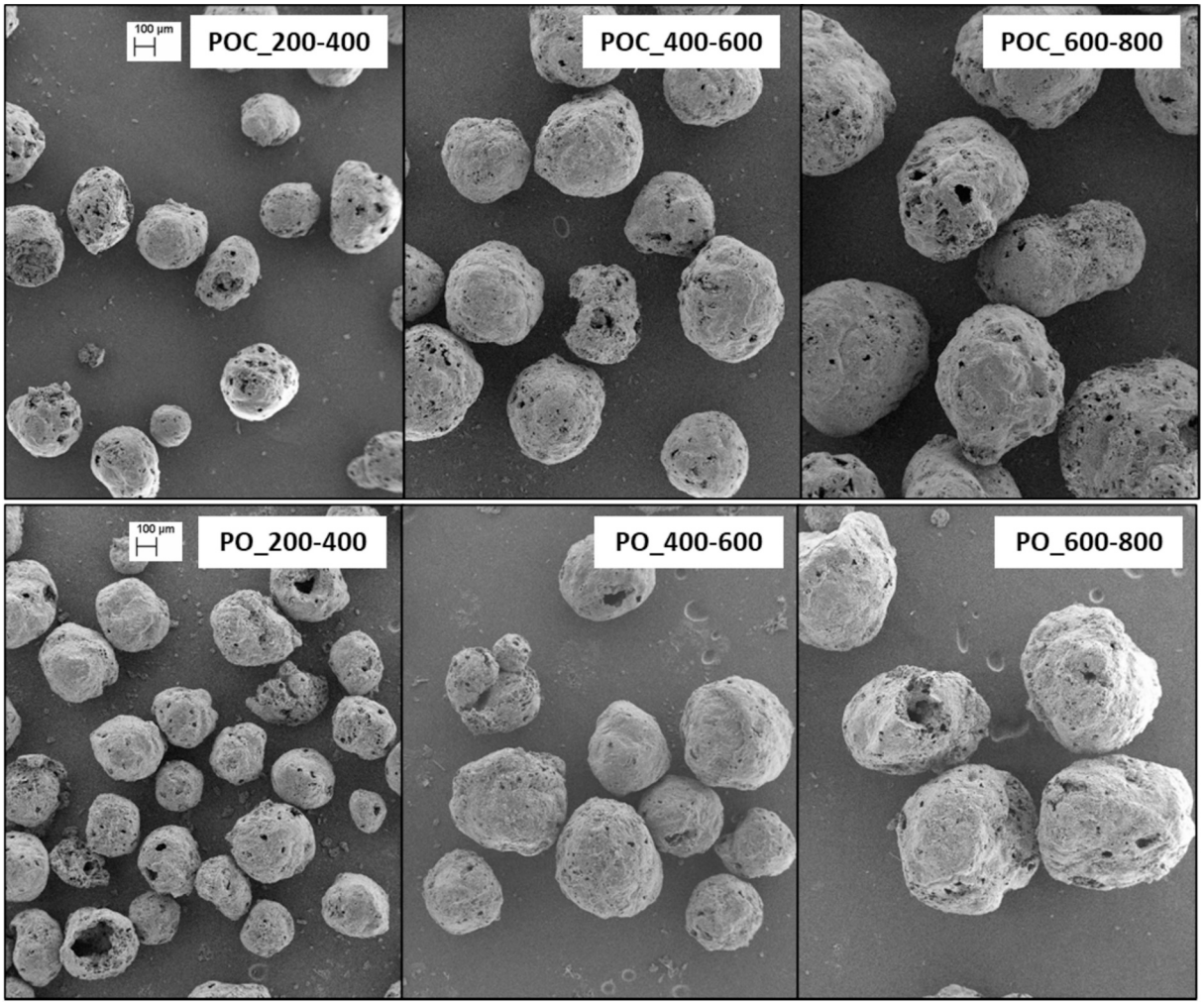

Fig. 3. SEM images of the size fractions of the samples produced during EFG experiment with POC (upper row) and with PO (lower row) (200 µm – 400 µm, 400 µm – 600 µm and 600 µm – 800 µm).

cenosphere from the POC experiment. The surface of the cenosphere (left side) exhibits bubble-like structures and openings in the micrometer size range. On the magnification on the right side of Fig. 4 (a), an embedded char particle (indicated by a red arrow) can be distinguished from the surface equally made of a solid matrix. This may support the observation made by Stoesser et al. for cenospheres from a POC feed, that cracked pyrolysis oil becomes the binder, keeping char particles together [13]. A fluffy substance covering the surface of the cenosphere can be seen on the right side of Fig. 4 (a). SEM-EDXS analyses revealed that these structures are composed of soot, accompanied by ash (see SEM-EDXS analyses in the supplementary material D). While soot originates from gas-phase reactions, ash originates from inherent inorganic matter of the biomass. Soot and ash may deposit on the cenospheres from the gas phase (slag can be present as fine slag particles as well as

Table 3
Proximate analyses in wt.-% of the sieved fractions of cenospheres of $d_{Particle} \geq 200\,\mu m$ after drying at 105 °C.

Feed	Size fraction	Ash	Volatile matter	Moisture	Fixed carbon
	µm		wt.-%		
POC	200 – 400	11.4	5.7	2.9	79.7
	400 – 600	9.5	6.3	3.2	80.9
	600 – 800	9.2	6.1	3.4	80.6
PO	200 – 400	4.9	11.5	1.0	82.5
	400 – 600	4.5	10.2	1.2	84.1
	600 – 800	3.5	8.9	2.1	85.4

Table 4
Ultimate analysis in wt.-% (elemental composition) of cenospheres of $d_{Particle} \geq 200\,\mu m$ (oxygen by difference).

Feed	Size fraction	C	H	N	S	O
	µm			wt.-% (daf)		
POC	200 – 400	93.9	0.7	0.7	0.2	4.5
	400 – 600	93.9	0.7	0.8	–	4.6
	600 – 800	93.8	0.9	0.9	–	4.5
PO	200 – 400	96.2	1.6	0.7	0.3	1.2
	400 – 600	96.9	1.4	0.9	0.3	0.6
	600 – 800	96.3	1.2	1.0	0.3	1.2

vaporized mineral species).

Exemplary µCT scans of the cenospheres from the POC experiment (fractions 200 – 400 µm and 400 – 600 µm) are presented in Fig. 4 (b). Internal structures of the cenospheres were measured using the Dragonfly software. No fundamental differences in internal structures could be found comparing the different cenosphere fractions. All cenospheres have cavities of different diameters, ranging from hollow to more compact porous spheres. Accordingly, shell thickness ranges from 50 µm to more than 100 µm. Char particles of up to 100 µm (encircled in white) dominate the internal structure of the POC cenospheres. As by means of the SEM images (4 (a)), openings stemming from blowholes or fractures can be found in the outer shell of the cenospheres (encircled in red).

Completely white areas of 10 µm – 50 µm correspond to glass beads, fragments of glass beads or slag fragments.

Fig. 4 (c) shows a cenosphere and the magnification of a PO cenosphere. Small bubble-like structures are visible on the surface of the PO cenospheres. The magnification reveals the presence of sponge-like skeletons and thin films besides more compact sponge-like structures. The PO cenospheres resemble cenospheres from liquid feed experiments reported in [6,8,11,13].

Fig. 4 (d) shows µCT scans of cenospheres from the PO experiment. As already observed for the POC cenospheres, PO cenospheres also show cavities of different sizes and blowholes (encircled in red). The internal structures do not change with particle size.

Overall, the principal structure of cenospheres from POC and PO experiments reveals common features. The newly created carbon matrix is porous and has a sponge-like structure. The cenospheres' internal structures vary from continuously porous to porous shells with one large cavity. In cenospheres from the POC experiment, the structure is overlaid with embedded char particles. Therefore, the cenospheres from the POC experiment appear more compact and the internal structure seems more edged because of the embedded char particles.

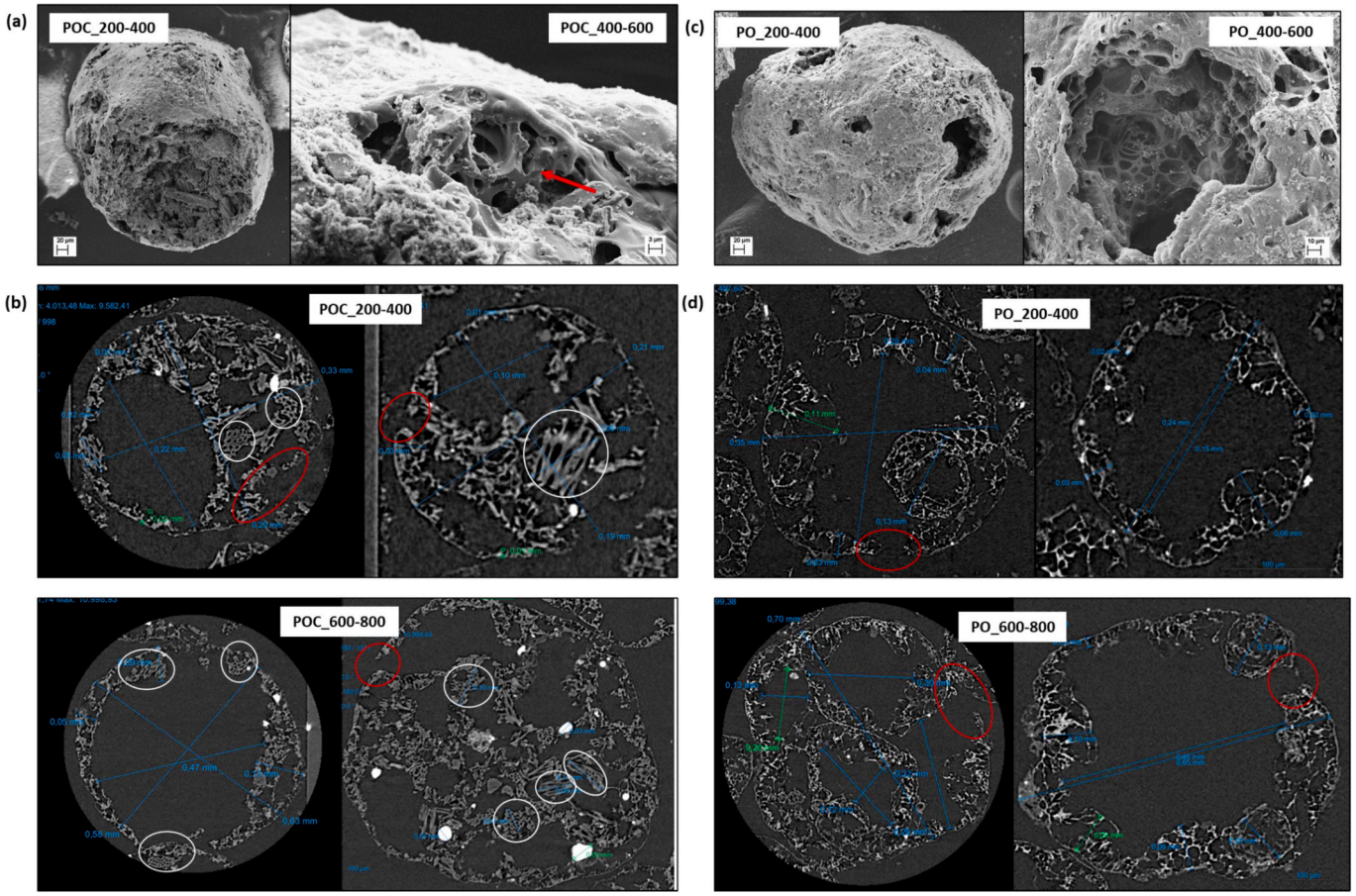

Fig. 4. SEM images (a) and µCT scans (b) of cenospheres found after the POC experiment and SEM images (c) and µCT scans (d) of cenospheres found after the PO experiment.

3.3. Pore size analysis and porosity calculations

3.3.1. Micro- and mesoporosity

Fig. 5 gives an overview of the micro- and mesopore surface areas of the sieving fractions of the POC and PO cenospheres determined by argon physisorption.

POC cenospheres exhibit pronounced microporosity. In comparison to the original beech wood char in the feed of the EFG experiment ($S_{micro} = 113\,m^2/g$), the micropore surface area of POC cenospheres is more than three times higher. The mesopore surface area of POC cenospheres is of the same order of magnitude as of the original beech wood char ($S_{meso} = 76\,m^2/g$).

In previous studies, beech wood char particles originating from the same batch as used in the POC feed of the EFG experiment were subjected to secondary pyrolysis under conditions comparable to those experienced by the POC cenospheres in the hot oxidation zone of the gasifier. The secondary pyrolysis was carried out in a drop-tube reactor at 1400 °C with a residence time of 200 ms in the hot zone, resulting in a comparably severe thermal treatment as that undergone by the POC droplets in the gasifier [21]. The char particles produced under these conditions exhibited a micropore surface area of $S_{micro} = 660\,m^2/g$ [21], which is of the same order of magnitude as that determined for the POC cenospheres.

PO cenospheres have no micropores, which is consistent with findings from [13]. The mesopore surface area of PO cenospheres is approximately one quarter of that of the POC cenospheres.

A plausible, though not yet verified explanation for the observed differences in micro- and mesopore surface area is that the microporosity and part of the mesoporosity can be assigned to the embedded char particles in the matrix of POC cenospheres. High heating rates undergone by the beech wood char particles in the POC droplets may have led to the formation of new micro- and eventually mesopores, as widely reported in literature [13,21,30,43].

Fig. 5 shows that principally, the specific micro- and mesopore surface areas decrease with increasing cenosphere diameter. In the case of POC cenospheres, it can be hypothesized that the reason for the decreasing micropore surface area with increasing cenosphere diameter could be a decreasing char particle content.

3.3.2. Macroporosity

Fig. 6 summarizes the results from pore analysis with OpenPNM. Pore diameters were normalized to the particle diameters. The relative frequency refers to the fraction of pores whose diameters fall within a given class of $d_{Pore}/d_{Particle}$. The sum of the relative frequencies over all pore size classes for a given particle equals 1.

The pore size distributions of all investigated particles follow very similar courses with pore diameters smaller than 10 % of the particle diameter being most frequent. Only few cavities with diameters corresponding to half the particle diameter could be found. However, largest cavities detected reached diameters of 88 % of the particle diameter. This generally confirms the findings in section 3.2. that the principal (macro-)structure of cenospheres from both experiments is similar.

The distribution in POC cenospheres shows greater variability compared to PO cenospheres. Possible explanations are that the presence of char particles on POC cenospheres influences the macropore distribution, as char particles typically exhibit cylindrical or slit-shaped macropores. These pores may be partially filled with the newly formed carbon matrix. Additionally, the presence of char particles may have affected the macropore formation during the cenosphere formation process. This may have led to a different macropore distribution compared to that of cenospheres derived from PO. For a conclusive explanation, however, a more comprehensive understanding of the formation processes as well as data obtained from a more representative particle set are required and will be addressed in future research.

3.3.3. Total porosity

Fig. 7 summarizes the results of the skeletal density measurements (helium pycnometry) as well as estimated particle porosities and densities (see section 2.4.4.). For all cenosphere types, skeletal densities lie in the range of 1.53 g/cm^3 to 1.86 g/cm^3. Estimated particle densities range from 0.26 g/cm^3 to 0.4 g/cm^3 and porosities vary in the narrow range of 0.76 – 0.85, a span also found for cenospheres from heavy fuel oil combustion [44].

The derived porosities and particle densities are used to calculate volumetric reaction rates required for an assessment of the influence of mass transport processes (see sections 3.5. and 4.).

3.4. Analysis of the carbon structure

Fig. 8 (a) shows the XRD diffractograms of POC_200-400, POC_600-800, PO_200-400 and PO_600-800. The first characteristic reflection at 24° 2θ attributed to the (002) plane (reflection at stacked graphene layers) as well as the second characteristic reflection at 44° 2θ ((100), reflection at aromatic ring structures within the layers) are clearly visible for all samples.

The diffractograms also contain narrow peaks that represent crystalline phases. The main difference in crystalline phases is the formation of calcite (C) in the POC cenospheres. As explained in section 3.1, a meaningful interpretation of the ash composition was not feasible. For a more detailed analysis of the crystalline inorganic phases detected via XRD, the reader is referred to the supplementary material D.

The coherence lengths L_a and L_c were refined from the coherent

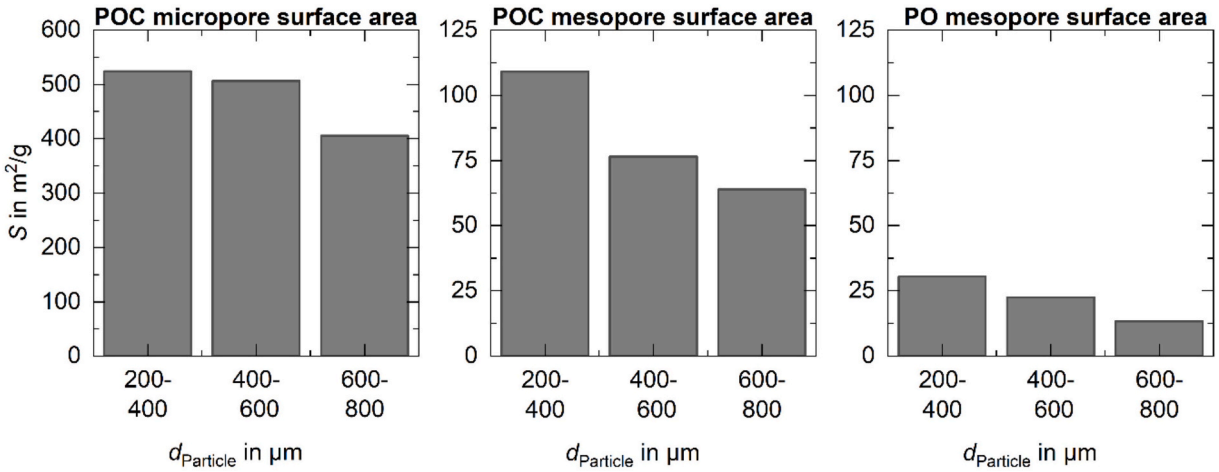

Fig. 5. Micropore and mesopore surface areas of the 200 – 400 µm, 400 – 600 µm and 600 – 800 µm fractions of POC and PO cenospheres.

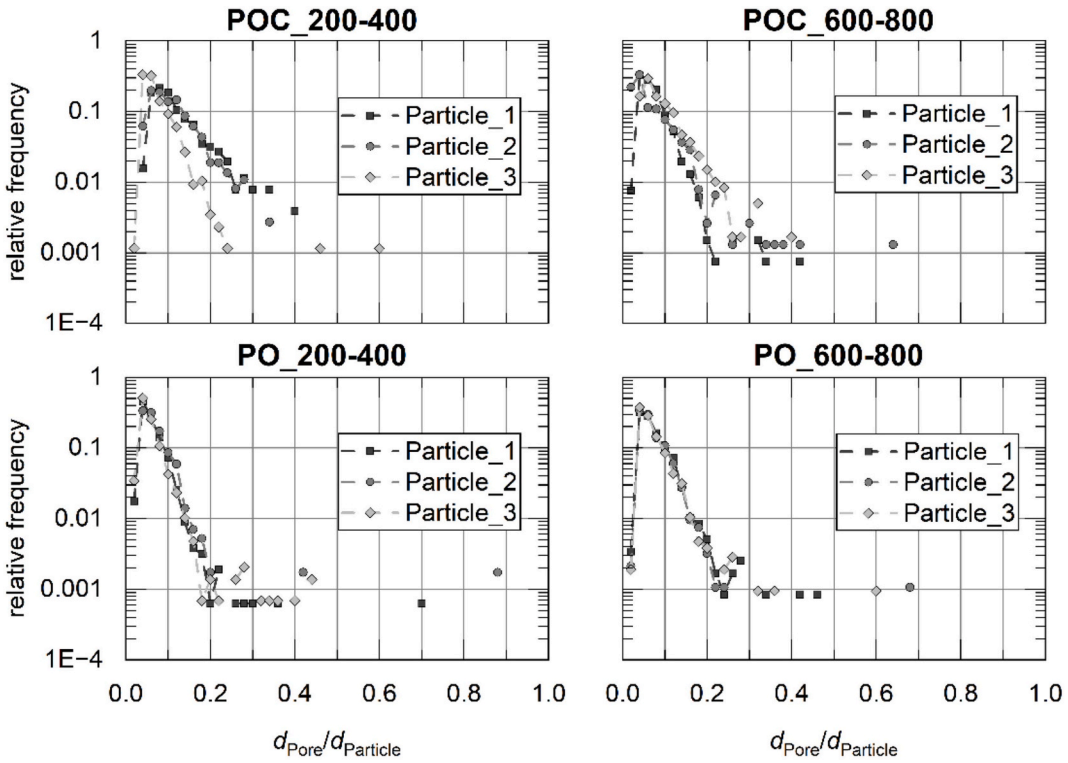

Fig. 6. Relative frequency of macropores in the micrometer size range from OpenPNM: pore diameters were normalized to the particle diameter. The labels 1, 2, and 3 refer to the three individual particles analyzed.

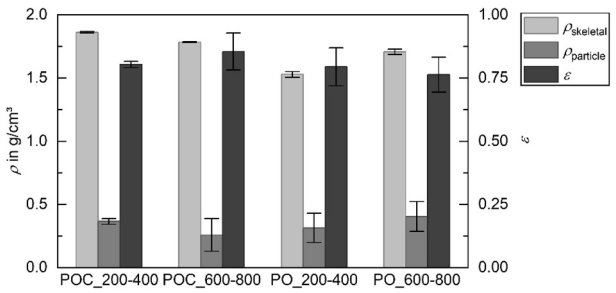

Fig. 7. Skeletal density, particle density and porosity.

scattering domain sizes corresponding to the (100) and (002) peaks, respectively. The results are depicted for all fractions of POC and PO cenospheres in Fig. 8 (b).

For the cenospheres from both EFG experiments, the interlayer spacing d_{Layers} does not change with particle diameter. The values of d_{Layers} found are high compared to literature data on the structure of graphite (3.354 Å [45] vs. 3.77 ± 0.001 Å (POC) and 3.66 ± 0.004 Å (PO)), indicating a generally low degree of stacking order within the graphene domains.

In the samples obtained from the POC experiment, the stacking coherence length L_c remains approximately constant across the investigated cenosphere sizes. The lateral coherence length L_a is higher in smaller cenospheres. Consequently, smaller cenospheres show a higher degree of in-plane structural ordering of the sp^2 carbon network, while the stacking height does not change with cenosphere diameters.

In contrast in PO cenospheres, both L_a and L_c are higher in the smaller fractions and show the trend to decrease with increasing diameter. Hence, analogously to POC cenospheres, an increasing degree of structural ordering with decreasing diameter can be stated.

In summary, distinct size-dependent trends in the geometric spreads of the graphene domains in POC and PO cenospheres can be stated: with increasing cenosphere diameter, POC cenospheres predominantly exhibit a decrease in L_a, whereas L_c additionally decreases in PO cenospheres. The presence of char particles seems to influence the geometry of structured domains in the carbon matrix (L_a vs. L_c).

This interpretation is tentatively supported by observations reported in [21], where increases in L_a were found to be associated with a higher degree of structural ordering in beech wood char particles.

Along this line of reasoning, the comparatively high L_a values observed for smaller POC cenospheres may therefore indicate an increased content of embedded char particles in these size fractions, although further research is required to substantiate this assumption.

In addition to the XRD measurements, Raman spectroscopy was also conducted with all size fractions (supplementary material B). Raman measurements confirmed the results and conclusions of the XRD measurements. Both XRD and Raman measurements on highly-disordered materials are challenging due to the overlap of broad bands and accompanying background issues [46]. However, both, XRD and Raman measurements revealed predominantly amorphous carbon as well as larger graphene stack and higher degree of structural ordering in the carbon matrix for smaller cenosphere fractions. Based on the validation by Raman spectroscopy, the trends observed by XRD were considered as significant.

3.5. Gasification experiments

Gasification temperatures below 900 °C correspond to the chemically controlled regime for wood char particles following [22]. Prior to the experiments, it was presumed that the temperature range for the chemically controlled regime was also valid for cenospheres. After the experiments, this presumption was verified through the Weisz-Prater criterion ψ (eq. (14)) [47].

$$\psi = \frac{r_{particle}^2 \cdot r_{V,eff}}{D_{Kn,eff} \cdot c_{CO_2,S}} \tag{14}$$

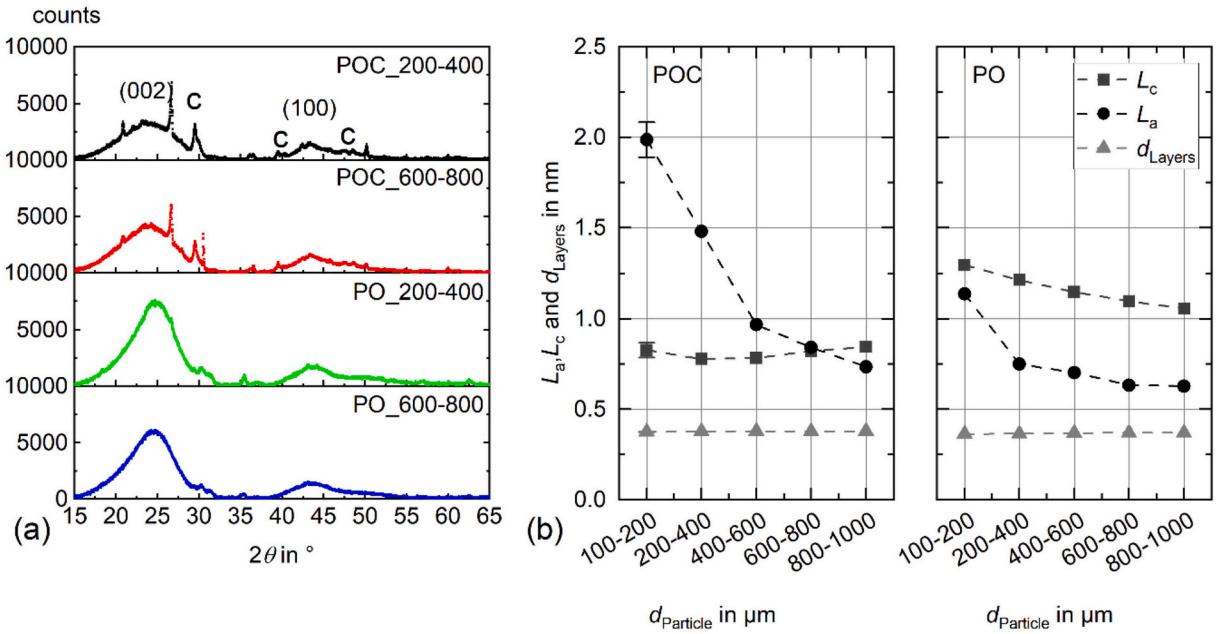

Fig. 8. X-ray diffractograms for cenosphere fractions 200 – 400 and 600 – 800 µm obtained during EFG experiments with POC and PO, calcite is marked (C) (a). Coherence lengths L_a and L_c as well as the interlayer spacing d_{Layers} in all fractions, with error bars from the repeated measurements on samples of POC_100-200 (b).

In eq. (12), the effective reaction rate $r_{V,eff}$ is experimentally determined, the particle radius $r_{particle}$ is the mean radius of the cenospheres size fraction, $D_{Kn,eff}$ is the effective Knudsen diffusion coefficient and $c_{CO_2,S}$ is the CO_2 concentration. The derivation of the parameters is explained in the supplementary material F. The influence of pore diffusion on the reaction rate can be neglected for Weisz moduli $\psi < 6$ for reaction orders of $n = 0$ and for $\psi < 0.6$ for reaction orders of $n = 1$ [47]. The Weisz moduli for the experiments at 850 °C are in the range of 0.04 to 1.94. As reaction orders n of the Boudouard reaction are reported in the range of 0.5 or below, it is concluded that mass transport has no significant influence for the investigated reaction temperatures. Furthermore, the characteristic diffusion length used in the Weisz modulus is the particle radius $r_{particle}$. This represents an extreme case for the cenospheres assuming evenly distributed porosity. Due to the presence of one larger internal cavity in most cenospheres (see section 3.3.2.), the diffusion length is smaller than the radius, suggesting that actual Weisz moduli are even smaller.

Fig. 9 (a) illustrates an exemplary course of a gasification experiment of sample POC_200-400 at $p_{CO_2} = 5$ bar and $T_{reaction} = 850\,°C$ together with the corresponding UCM fit (following equation (9), section 3.1.). In the beginning of the experiment, y_{CO} is highest but experiences a steep decrease up to $X_{C,gasif} \approx 0.3$. The decrease of the CO concentration is less steep until $X_{C,gasif} \approx 0.8$, then the concentration drops more rapidly until it reaches zero. Comparable courses were found for PO_200-400 and PO_600-800, as can be seen by means of Fig. 9 (b), showing the conversion rates ($dX_{C,gasif}/dt$ vs. $X_{C,gasif}$) of all investigated samples for $p_{CO_2} = 5$ bar and $T_{reaction} = 850\,°C$. The described non-linear, three-step

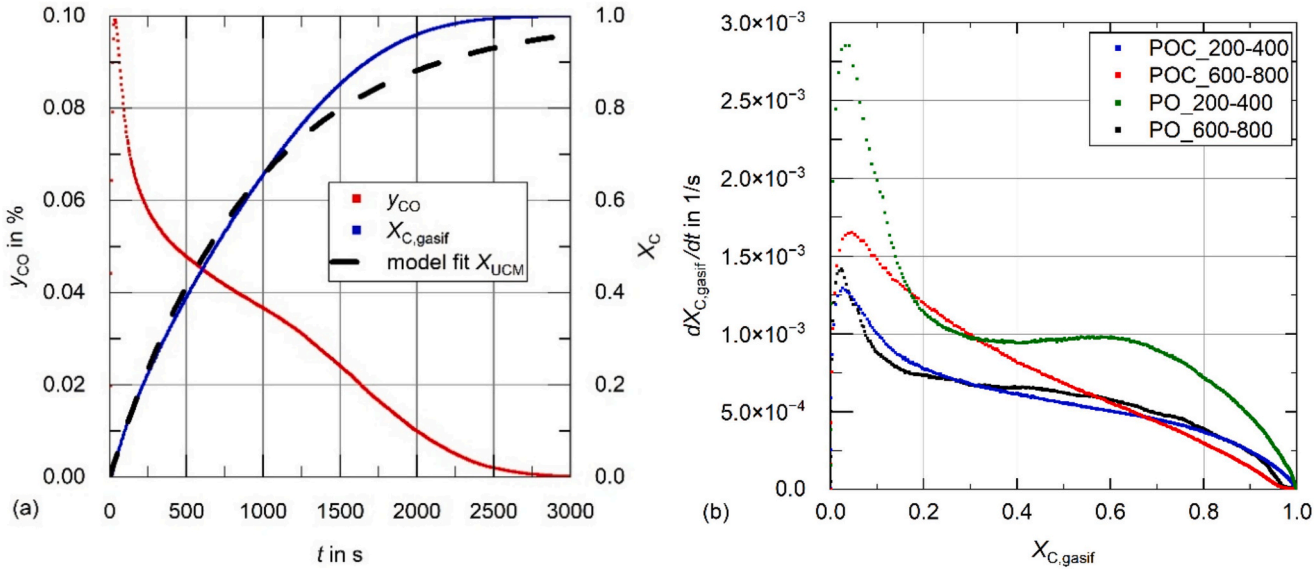

Fig. 9. (a) Gasification of cenospheres POC_200-400 at $p_{CO2} = 5$ bar and T = 850 °C. CO concentration y_{CO}, carbon conversion $X_{C,gasif}$ and UCM fit. (b) Conversion rates $dX_{C,gasif}/dt$ over conversion $X_{C,gasif}$ for POC_200-400, POC_400-600, PO_200-400 and PO_400-600 of the gasification experiment at $p_{CO2} = 5$ bar and $T_{reaction} = 850$ °C.

curve profile is very pronounced for PO_200-400, characterized by a high initial conversion rate and a roughly constant conversion rate for $0.3 \leq X_{C,gasif} \leq 0.6$. In the case of POC_600-800, the conversion rate decreases linearly. In contrast to the three-step curve profile of POC_200-400, PO_200-400 and PO_600-800, the linear behavior of $dX_{C,gasif}/dt$ of POC_600-800 exactly fits the UCM model.

As discussed in [39], a three-step curve profile may generally result from the evolution of the reactive and the catalytically active surface area during conversion. In [39], the impact of the deviation of the experimentally derived conversion rate from the model behavior of the UCM on the resulting reaction rate was assessed, with the clear result that for large fitting ranges of $X_{C,gasif}$ such as 5 – 80 %, the error is negligible.

Additionally, residual plots of the UCM model fitting for the given examples (Fig. 9, b) accompanied by a short discussion are given in the supplementary material G.

The reaction rates determined at $810\,°C \leq T_{reaction} \leq 850\,°C$ and $5\,bar \leq p_{CO_2} \leq 20\,bar$ are depicted in Fig. 10. For comparison, the power law model describing the reaction rates of the secondary beech wood char produced at 1400 °C is also given (experimental data published in [20]). The secondary char was already mentioned in section 3.3.1.

Former research demonstrated that the total pressure has negligible influence on the CO_2 gasification kinetics [48]. Within this research group, Schneider et al. investigated the influence of total pressure on the gasification kinetics in CO_2 using a previous version of the dFBR [20]. Consistent with findings reported by other research groups, their study demonstrated that total pressure does not significantly affect the intrinsic kinetics of CO_2 gasification. To provide additional certainty, the influence of total pressure ($p_{tot} = 20\,bar$) on the reaction rate (for $p_{CO_2} = 10\,bar$) was assessed by means of PO_200-400. The data point is included in Fig. 10. (grey data point). It can be seen that the data point lies within the range of the experimental error, so the influence of total pressure is negligible.

The adapted PL models are included in Fig. 10. with dashed lines.

Table 5 summarizes the PL model parameters. Especially the activation energies lie within a narrow range of $209.5\,kJ/mol \leq E_A \leq 241.8\,kJ/mol$. The partial pressure dependence of the reaction rate, expressed by the reaction order n, also lies within a narrow range of 0.199 – 0.305.

This indicates comparable values of the parameters of the CO_2 kinetics modeled with a power law and Arrhenius model as found for the beech wood char particles introduced in section 3.3 after comparably severe heat treatment in a drop-tube reactor at 1400 °C for 200 ms [21], which were $E_A = 309\,kJ/mol$ and $n = 0.214$ [20].

The values of E_A also correspond well to the findings of Cetin et al. [49] for atmospheric gasification of fast-pyrolysis biomass chars in a thermogravimetric analyzer (bagasse, pine and eucalyptus, pyrolyzed at heating rates of 500 K/s). Activation energies lay in the range of $198\,kJ/mol \leq E_A \leq 238\,kJ/mol$. Li et al. [50] investigated CO_2 gasification kinetics of coal chars up to CO_2 partial pressures of 10 bar and 900 – 1000 °C. The kinetics were modeled with the shrinking core model and the power law model. Resulting reaction orders were $0.26 \leq n \leq 0.5$ and activation energies were $114\,kJ/mol \leq E_A \leq 209\,kJ/mol$ [50].

The parameters found for POC and PO cenospheres correspond to the mentioned results despite the different fuel types (fossil coal char, biochar vs. cenospheres created form biogenic pyrolysis oil and suspensions). This indicates that the derived kinetics are micro-kinetics and further substantiates that the gasification experiments were conducted in the chemically controlled regime.

Besides the PL model, also the Langmuir-Hinshelwood (LH) model was adjusted to the experimental reaction rates. The LH model described the reaction rates accurately as well. The LH model parameters and parity plots of both kinetic models are given in the supplementary material G.

A comparison of the experimental reaction rates of the cenospheres

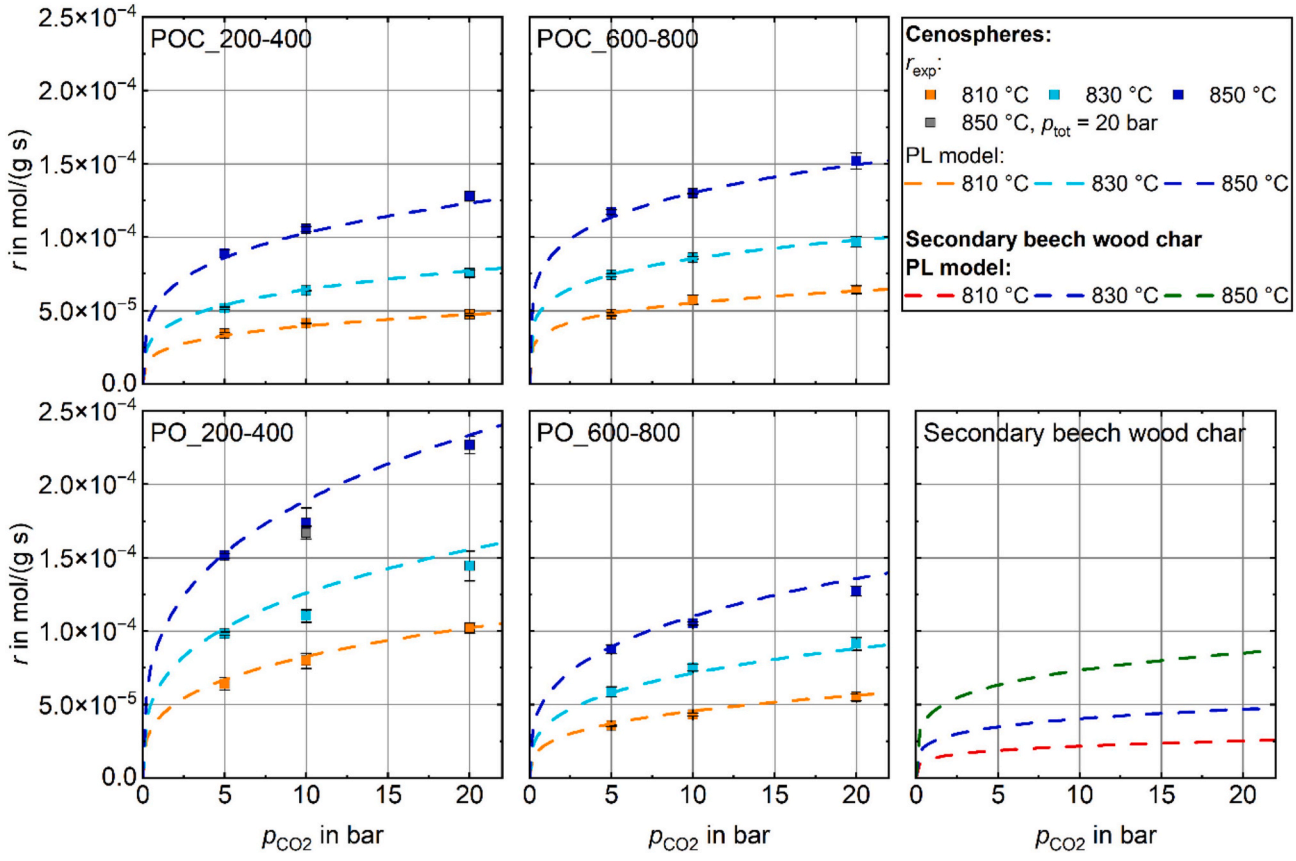

Fig. 10. Reaction rates of the Boudouard reaction of cenospheres POC_200-400, POC_400-600, PO_200-400 and PO_400-600 and corresponding power law models as well as power law model for secondary beech wood char [20].

Table 5
Parameters of the PL and Arrhenius model used to describe the reaction rates of the investigated cenosphere size fractions as well as model parameters of secondary beech wood char for comparison [20].

	POC_200-400	POC_600-800	PO_200-400	PO_600-800	Secondary beech wood char [20]
k_{0,CO_2} in mol g^{-1}s^{-1}bar^{-n}	$1.02{\cdot}10^{7}$	$1.02{\cdot}10^{6}$	$4.92{\cdot}10^{5}$	$1.20{\cdot}10^{6}$	$1.02{\cdot}10^{10}$
E_{A,CO_2} in kJ mol^{-1}	241.8	216.9	209.5	223.2	308.7
n_{CO_2}	0.259	0.199	0.305	0.303	0.214

in Fig. 10. shows that the reaction rates of POC cenospheres (both fractions) and PO_600-800 fall within a similar range, while PO_200-400 shows substantially higher reaction rates.

The secondary char particles react significantly slower than the cenospheres formed during both EFG experiments. Accordingly, the solid carbon matrix that was newly created is more reactive than the secondary beech wood char matrix. A comparison of the results of the XRD analyses of the cenospheres with those of the secondary char ($L_a \approx 2.9$ Å, $L_c \approx 1.1$ Å, $d_{Layers} \approx 3.9$ Å [21]) reveals that structured domains in the secondary char matrix are larger than those observed in the cenospheres. This may explain the lower reaction rates.

The investigated cenospheres differ in both specific surface area and structural ordering (as reflected by variations in L_a and L_c), which complicates the direct correlation of reaction rates with these char properties. Therefore, a simplified structural parameter (A/V), equation (15), derived from the XRD results, was introduced to condense the influence of structural ordering on the micro-kinetics into a single parameter. The carbon structure is represented by graphene domains consisting of stacked layers with finite lateral and stacking coherence lengths. While C atoms located at the edges are reactive, C atoms within the basal planes remain largely inert. Therefore, the ratio of edge to basal plane sites (A/V) was approximated from the coherence lengths L_a and L_c. Thus for simplicity, the graphene stacks were approximated as cylinders for this calculation. High ratios (A/V) correspond to a higher number of reactive C atoms per char surface, thus should correspond to higher surface specific reaction rates. Since from the literature, it is known that the micropore surface area only marginally contributes to the C-CO_2 reaction [51–53], the reaction rate in CO_2 is referred to the mesopore surface area (eq (16)).

$$\frac{A}{V} = \frac{\textit{mantle area of a cylinder}}{\textit{volume of a cylinder}} = \frac{\pi \cdot L_a \cdot L_c}{\frac{1}{4}\cdot\pi\cdot L_a^2 \cdot L_c} = \frac{4}{L_a} \tag{15}$$

$$r_{meso} = \frac{r}{S_{meso}} \tag{16}$$

Fig. 11 shows the surface specific reaction rate r_{meso} over the ratio (A/V).

A strong correlation between r_{meso} and (A/V) can be stated by means of Fig. 11. To underline the trend of increasing r_{meso} with increasing (A/V), a fit of the form $r_{meso} = a{\cdot}(A/V)^b$ is also given in Fig. 11. The approach $r_{meso} = a{\cdot}(A/V)^b$ was chosen because of the simplicity; the functional form (power law) and parameters a and b have no physical meaning.

At this stage, it should be noted that the underlying reasons for the observed values of the structural parameters L_a and L_c, and the micro- and mesopore surface areas cannot yet be conclusively identified. It is conceivable that knowledge of the time–temperature-history of the cenospheres could provide an explanation. Such analysis, however, is beyond the scope of the present work and will be addressed in the future.

4. Discussion on the derived reaction kinetics in the context of EFG conditions

In the present study, cenospheres were obtained for the first time from experiments conducted in the bioliq pilot-scale entrained flow reactor. The cenospheres were classified into size fractions, characterized, and their reaction kinetics in CO_2 were investigated. However, for the transfer to technical systems operated at high temperatures, it is of fundamental importance to evaluate the role of mass transport through the film surrounding the particle and the particle's inner pore structure, as they significantly influence the effective reaction rate and therefore the carbon conversion achieved during EFG. This is of special interest with respect to the morphology of cenospheres (particularly particle diameter and inner pore structure), that largely differs from the morphology of char particles.

Since no experiments on the influence of mass transport on the effective reaction rate under EFG conditions have been conducted, a parameter study considering temperature, particle type (POC or PO cenospheres), particle diameter and internal structure (one large cavity vs. evenly distributed inner porosity) was carried out. For the different

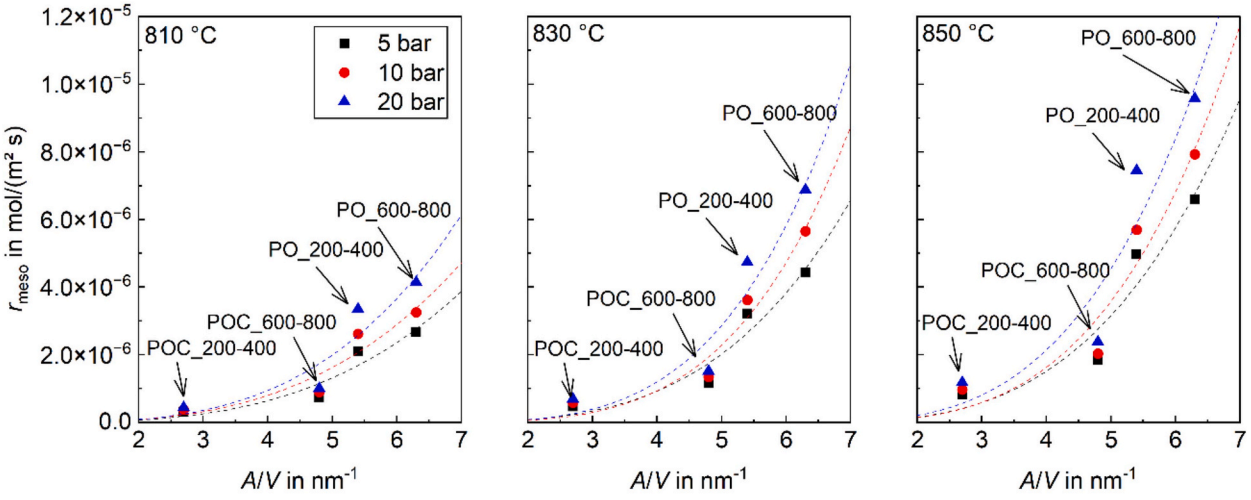

Fig. 11. Reaction rates r_{meso} of the cenosphere fractions 200 – 400 µm and 600 – 800 µm of POC and PO cenospheres for 810 – 850 °C and 5 – 20 bar related to the mesopore surface area over ratios (A/V).

particle types and diameters, the reaction kinetics determined in this work were used. Given that kinetic data were only available for the Boudouard reaction, the parameter study was restricted to the CO-CO_2 system (with technically relevant partial pressures $p_{CO} = p_{CO_2} = 10$ bar). As Stoesser found that for high pressure conditions, product gas inhibition plays a minor role, product inhibition was not considered [54]. Table 6 summarizes the parameter variation.

The commonly used simple mass balance coupling film diffusion, pore diffusion and reaction (eq. (17)) was iteratively solved for each combination of parameters.

$$r_{eff} = \beta_{CO_2} \cdot \left(c_{CO_2,Bulk} - c_{CO_2,S}\right) \cdot S_{diff} = \eta \cdot k_V \cdot c^n_{CO_2,S} \cdot V_{particle} \quad (17)$$

In eq. (17), the effective reaction rate r_{eff} corresponds to the film diffusion through the diffusion surface S_{diff} driven by the concentration gradient and described by the mass transport coefficient β_{CO_2} as well as to the coupled pore diffusion and reaction, which is described by the pore effectiveness factor η.

Since no particle conversion model was integrated in eq. (17), the resulting effective reaction rates r_{eff} and pore effectiveness factors η only apply to the initial stage of conversion.

For the diffusion through the film surrounding the cenospheres, minimum Sherwood number $Sh_{min} = 2$ is assumed since particles follow the gas flow. The diffusion through the pores, coupled with the reaction at the inner surface, was described with the Thiele modulus. The generalized Thiele modulus Φ_{gen} is well-known (eq. (18)).

$$\Phi_{gen} = \frac{V_{particle}}{S_{particle}} \cdot \sqrt{\frac{n+1}{2} \cdot k_V \cdot \frac{c^{n-1}_{CO_2,S}}{D_{pore}}} = \frac{r_{particle}}{3} \cdot \sqrt{\frac{n+1}{2} \cdot k_V \cdot \frac{c^{n-1}_{CO_2,S}}{D_{pore}}} \quad (18)$$

µCT analyses showed that the internal structure of cenospheres ranges from an evenly distributed pore structure with small cavities to a porous shell with one large cavity with a diameter of up to 88 % of the particle diameter. The generalized Thiele modulus cannot describe mass transport in a shell-like structure. To account for the influence of large cavities, the Thiele modulus following Buffham with a reduced characteristic length of diffusion was calculated (eq. (19)) [55].

$$\begin{aligned}\Phi_{Buffham} &= \frac{V_{particle}}{S_{particle+cavity}} \cdot \sqrt{\frac{n+1}{2} \cdot k_V \cdot \frac{c^{n-1}_{CO_2,S}}{D_{pore}}} \\ &= \frac{\frac{4}{3} \cdot \pi \cdot \left(r^3_{particle} - r^3_{cavity}\right)}{4\pi \cdot \left(r^2_{particle} + r^2_{cavity}\right)} \cdot \sqrt{\frac{n+1}{2} \cdot k_V \cdot \frac{c^{n-1}_{CO_2,S}}{D_{pore}}}\end{aligned} \quad (19)$$

The radius r_{cavity} of the largest cavity observed from µCT measurements is $0.88\, r_{particle}$. It follows that $\Phi_{Buffham} = 0.18\, \Phi_{gen}$. $\Phi_{Buffham}$ and Φ_{gen} can be regarded as limiting cases, with any inner cavity smaller than $0.88\, r_{particle}$ resulting in $0.18\, \Phi_{gen} \leq \Phi \leq \Phi_{gen}$. For the temperature range regarded, Knudsen diffusion is the dominant diffusion mechanism in micro- and mesopores up to a diameter of 9 – 15 nm. Since the small pores mainly contribute to the specific surface area, the effective diffusion coefficient D_{pore} was calculated for the Knudsen diffusion mechanism.

Fig. 12 (a) summarizes the effective reaction rates (in mol/m³/s) calculated with Φ_{gen} (row one) and $\Phi_{Buffham}$ (row two) as well as pore effectiveness factors $\eta_{Knudsen}$ for 1000 °C and 1500 °C. Fig. 12 (b) exemplarily depicts an Arrhenius diagram for POC_200 and for the beech wood char particles of on average 75 µm (50 – 100 µm) introduced in section 3.3 and investigated in [20].

Effective reaction rates of the cenospheres with the generalized Thiele modulus Φ_{gen} (Fig. 12 (a), row one) are strongly influenced by pore diffusion at 1000 °C as pore effectiveness factors are low. At 1000 °C, effective reaction rates appear to lie just within the pore diffusion controlled regime following Rossberg and Wicke [56]. The cenosphere diameter determines the diffusion length and therefore influences the reaction rate. Consequently, pore effectiveness factors are lower for larger cenospheres (POC_200 vs. POC_400, POC_600 vs. POC_800 etc.), indicating a stronger limitation by pore diffusion.

The sharp rise of $\eta_{Knudsen}$ between POC_400 and POC_600 can be attributed to the lower reaction rate found for the smaller fraction of POC_200-400.

For temperatures of 1500 °C, the transition to limitation of the outer mass transport is found (regime 3 following Rossberg and Wicke [56]). Then, pore effectiveness factors are close to zero and film diffusion is dominant, further increasing the impact of the particle diameter on the effective reaction rate. For a temperature of 1500 °C, film diffusion control should be considered for particle conversion modelling.

The Arrhenius diagram in Fig. 12 (b) allows for a comparison between the macro-kinetics of the secondary beech wood char [20] and the POC_200. For POC_200, both Φ_{gen} and $\Phi_{Buffham}$ were considered.

The Arrhenius plots of POC_200 (Φ_{gen}) and the secondary beech wood char show the typical, well-known shape with three distinguishable regimes following Rossberg and Wicke [56]. The transitions from regime 1 to 2 and 2 to 3 can be observed at similar temperature ranges for the secondary beech wood char and POC_200 (Φ_{gen}). In contrast, the macro-kinetics of POC_200 ($\Phi_{Buffham}$) follow a very different trend. Notably, the transitions from regime 1 to 2 and 2 to 3 modeled with $\Phi_{Buffham}$ are in close proximity and cannot be clearly distinguished in the Arrhenius plot. Compared to cenospheres with continuous porosity, the transition from regime 1 to 2 shifts towards higher temperatures for cenospheres with one large cavity. Due to the higher effective reaction rates, film diffusion comes into effect at lower temperatures. This observation is explained by the reduced characteristic length of diffusion.

Typical temperatures in technical entrained flow gasifiers range above 1200 °C and result in low pore effectiveness factors of below 0.04 and a significant limitation of film diffusion for all particle types investigated. Especially the large particle size distribution of the analyzed cenosphere samples leads to a broad distribution of effective reaction rates at EFG conditions.

Besides Knudsen Diffusion, also molecular diffusion in macropores was assessed. As film diffusion and pore diffusion then follow the same mechanism, they also become limiting at the same temperature and only a transition from the chemically controlled regime 1 to a diffusion controlled regime can be found. Further information on the calculation basis for the parameter study as well as a more details on the diffusion in macropores and can be found in the supplementary material F.

Table 6
Parameters and ranges / values for the parameter study on the influence of mass transport on the effective reaction rate.

Parameter	Range / values
Temperature in °C	1000, 1500
Particle type	POC, PO
Cenosphere diameter in µm	200, 400, 600, 800 (the same kinetics were applied to the diameters of 200 µm and 400 µm as well as 600 µm and 800 µm)
Diffusion mechanism	Knudsen diffusion
Internal structure	Evenly distributed porosity, one large cavity ($0.88\, r_{particle}$)

5. Summary and conclusion

Cenospheres with a wide particle size distribution of 200 – 800 µm were produced from entrained flow gasification (EFG) experiments at 40 bar in the bioliq entrained flow gasifier with beech wood pyrolysis oil (PO) and suspensions of pyrolysis oil and beech wood char particles (POC) under low air ratios of 0.35. The cenospheres were characterized in order to generate data for EFG numerical simulation to take account for cenospheres as intermediates in the gasification process.

Micro computer tomography revealed a generally sponge–like structure of the cenospheres, which is either continuous or contains larger internal cavities. In POC cenospheres, this structure is overlaid by embedded char particles. Cenospheres obtained from POC and PO

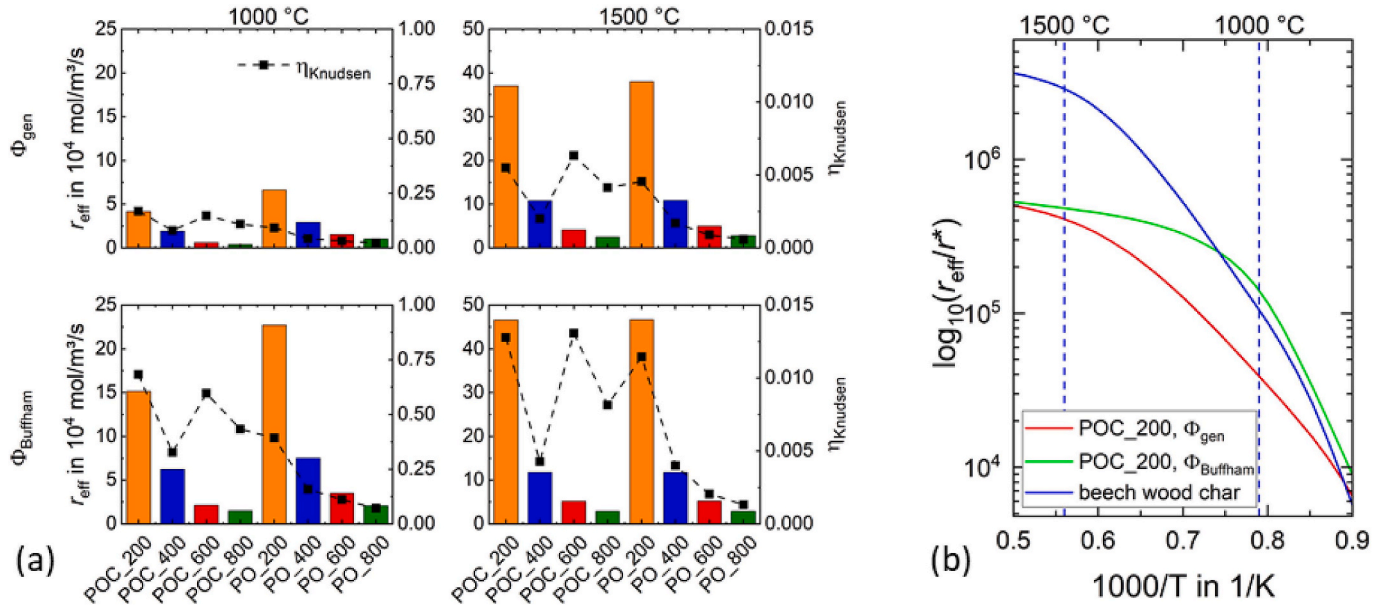

Fig. 12. Effective reaction rates for different cenosphere diameters for cenospheres from EFG experiment with POC and PO with evenly distributed porosity (row one, Φ_{gen}) and for cenospheres with one large cavity of 0.88 $r_{Particle}$ (row two, $\Phi_{Buffham}$), Knudsen diffusion in the pores and film diffusion (molecular diffusion) (a) and Arrhenius diagram for POC_200 (b).

experiments both exhibit mesoporosity. Cenospheres with embedded char particles exhibit pronounced microporosity and larger specific surface area compared to PO cenospheres.

From X-ray diffraction, a generally lower degree of structural ordering (graphitization) compared to char particles with a similar time–temperature history was found for the cenospheres. For both cenosphere types (with and without char particles), structural ordering increased with decreasing diameter. Additionally, with decreasing diameter, the coherence lengths of the structured domains followed distinct trends in POC and PO cenospheres, with larger graphene layers in POC cenospheres and both larger graphene layers and increased stacking in PO cenospheres.

The micro-kinetics of two size fractions (200 – 400 μm and 600 – 800 μm) at 810 – 850 °C and at 5 – 20 bar CO_2 partial pressures were investigated in the differential fixed bed reactor. The reaction rates could be described with the Arrhenius approach, combined with the power law model.

The reaction rates of POC_600–800, PO_600-800 and POC_200-400 resulted to lie within a narrow range, while PO_200–400 exhibited higher reaction rates. This finding correlates well with the ratio of C atoms located at the edges (reactive) to C atoms within the basal planes (unreactive) derived from and the mesopore surface area.

Finally, estimations of mass transport under EFG conditions indicated that cenosphere conversion predominantly occurs in the film diffusion-controlled regime.

Further research should focus on the formation process of cenospheres under conditions of technical entrained flow gasifiers, provide a dynamic model to describe structure-resolved particle conversion coupled with mass transport and investigate the gasification kinetics of cenospheres in steam and steam-CO_2 mixtures.

CRediT authorship contribution statement

Stella Walker: Writing – original draft, Visualization, Validation, Supervision, Software, Methodology, Investigation, Formal analysis, Conceptualization. **Manuel Nather:** Writing – original draft, Validation, Methodology, Investigation. **Angela Ullrich:** Methodology, Validation, Investigation, Writing – original draft. **Zahra Ghasemi Monfared:** Writing – review & editing, Methodology, Investigation. **Kentaro Umeki:** Writing – review & editing, Supervision. **Thomas Kolb:** Writing – review & editing, Supervision.

Declaration of competing interest

The authors declare that they have no known competing financial interests or personal relationships that could have appeared to influence the work reported in this paper.

Acknowledgements

The authors gratefully acknowledge the financial support by the Helmholtz Association of German Research Centers (HGF), within the research program Materials and Technologies for the Energy Transition (MTET) and the Swedish Research Council (Project number 2023-04185). Further acknowledgement goes to the operating team of the bioliq plant under the leadership of Bernd Zimmerlin and Bernd Michelfelder (KIT, Institute for Technical Chemistry, Energy Laboratories) for conducting the campaigns, to Ulrike Santo (KIT, Institute of Technical Chemistry), Manuel Haas (KIT, Institute of Technical Chemistry) and Maximilian Dammann (formerly KIT, Institute of Technical Chemistry) for fruitful discussions and their continuous collaboration and to Paul Moog (KIT) and Kamen Iliev (KIT) for their experimental support.

Glossary

Symbols

Symbol	Description	Unit (SI)
ad	air-dried	
(A/V)	mantle area-to-volume ratio	1/m
d	diameter/distance	µm
D	diffusion coefficient	m^2/s
d_{10}	10 % quantile	
d_{90}	90 % quantile	
daf	dry ash free	
E_A	activation energy	kJ/mol
I	intensity	
k	rate constant for kinetic models	variable
k_0	Pre-exponential factor for Arrhenius approach	variable
L	coherence length	Å or nm
m	mass	mg, g, kg
$\tilde{M}$	molar mass	g/mol
n	reaction order	–
p	pressure/partial pressure	bar
r	reaction rate	Mol/g/s or $mol/m^3/s$
R	reactivity	1/s
R^2	Coefficient of determination	
R_U	universal gas constant (8.314 J/mol/K)	J/mol/K
S	specific surface area	m^2/g
Sh_{min}	minimum Sherwood number	
T	temperature	°C or K
V	mass-specific volume	mm^3/g and cm^3/g
$\ddot{V}$	volume related to one particle	mm^3 or m^3
$\dot{V}$	volume flow	m^3/s
x	mass fraction	Wt.-%
X	conversion	
β	mass transport coefficient	m/s
ε	porosity	
λ	air ratio	
ϱ	density	g/cm^3
Φ	Thiele modulus	
ψ	Weisz modulus	

Subscripts

Subscript	Description
a	Stacking height of graphene layers
ash	ash
Buffham	calculated following Buffham [55]
Bulk	bulk gas phase
c	radial expansion of graphene layers
C	carbon
C,fix	fixed carbon
cavity	refers to the largest cavity in the cenospheres
D	D1 peak
diff	diffusion surface
G	G peak
gasif	total amount of gasified carbon
gen	generalized
i, j	summation index, iteration index
Knudsen	Knudsen diffusion
Layers	graphene layers
macro	macropore
meso	mesopore
micro	micropore
micro-meso	micropores and mesopores
Moisture	moisture
S	external particle surface
particle	particle
pore	pore
reaction	gasification experiment
sample	refers to the sample
sat	saturation vapor pressure
skeletal	skeletal density
tot	total
UCM	Uniform Conversion Model

(*continued on next page*)

(*continued*)

Subscript	Description
V	volumetric
vol	volatiles

Abbreviations

Abbreviation	Description
µCT	micro computer tomography
BET	Brunauer, Emmett, Teller
CFD	computational fluid dynamics
daf	dry ash free
dFBR	differential fixed bed reactor
EDXS	Energy-dispersive X-ray spectroscopy
EFG	entrained flow gasification
KIT	Karlsruhe Institute of Technology
LTU	Luleå University of Technology
LEM	Laboratory for Electron Microscopy
LH	Langmuir-Hinshelwood
OpenPNM	Open Pore Network
PL	power law
PO	Biogenic pyrolysis oil
POC	Suspension of biogenic pyrolysis oil with char
QSDFT	Quenched Solid Density Functional Theory
SEM	Scanning electron microscopy
UCM	Uniform Conversion Model
wt.	weight
XRD	X-ray diffraction

Appendix A. Supplementary data

Supplementary data to this article can be found online at https://doi.org/10.1016/j.fuel.2026.140731.

Data availability

Data will be made available on request.

References

[1] Ranjbar N, Kuenzel C. Cenospheres: a review. Fuel 2017;207:1–12. https://doi.org/10.1016/j.fuel.2017.06.059.

[2] Matsuoka K, Akiho H, Xu W, Gupta R, Wall TF, Tomita A. The physical character of coal char formed during rapid pyrolysis at high pressure. Fuel 2005;84:63–9. https://doi.org/10.1016/j.fuel.2004.07.006.

[3] Jarvis MW, Haas TJ, Donohoe BS, Daily JW, Gaston KR, Frederick WJ, et al. Elucidation of biomass pyrolysis products using a laminar entrained flow reactor and char particle imaging. Energy Fuels 2011;25:324–36. https://doi.org/10.1021/ef100832d.

[4] Jiang L, Elbaz AM, Guida P, Al-Noman SM, AlGhamdi IA, Saxena S, et al. Cenosphere formation during single-droplet combustion of heavy fuel oil. Energy Fuels 2019;33:1570–81. https://doi.org/10.1021/acs.energyfuels.8b03632.

[5] Moszkowicz P, Witzel L, Claus G. Modelling of very fast pyrolysis of heavy fuel oil droplets. Chem Eng Sci 1996.

[6] David Urban, Frederick Dryer (Eds.), New results on coke formation in the combustion of heavy-fuel droplets, 1990.

[7] Ganji MJZ, Ghassemi H. Evaluation of the solid particle from heavy fuel oil and its formation trend. Powder Technol 2023;427:118744. https://doi.org/10.1016/j.powtec.2023.118744.

[8] Setyawan HY, Zhu M. Cenosphere formation and combustion characteristics of single droplets of vacuum residual oils. Combust Sci Technol 2025;197:59–76. https://doi.org/10.1080/00102202.2023.2170750.

[9] Bomo N, Lahaye J, Prado G, Claus G. Formation of cenospheres during pyrolysis of residual fuel oils. 20th Symposium on Combustion/The Combustion Institute. 1984.

[10] Marrone NJ, Kennedy IM, Dryer FL. Coke formation in the combustion of isolated heavy oil droplets. Combust Sci Technol 1984;36:149–70. https://doi.org/10.1080/00102208408923731.

[11] Wornat MJ, Porter BG, Nancy YC. Yang, single droplet combustion of biomass pyrolysis oils. Energy Fuels 1994.

[12] Calabria R, Chiariello F, Massoli P. Combustion fundamentals of pyrolysis oil based fuels. Exp Therm Fluid Sci 2007;31:413–20. https://doi.org/10.1016/j.expthermflusci.2006.04.010.

[13] Stoesser P, Ruf J, Gupta R, Djordjevic N, Kolb T. Contribution to the understanding of secondary pyrolysis of biomass-based slurry under entrained-flow gasification conditions. Energy Fuels 2016;30:6448–57. https://doi.org/10.1021/acs.energyfuels.6b00935.

[14] Mohanty R, Mahanta P, Sharma RP. Recent advances in biomass gasification to improve the quality of syngas: a comprehensive review. Ind Eng Chem Res 2025;64:13950–65. https://doi.org/10.1021/acs.iecr.5c01388.

[15] Ullmann's Enzyklopädie: Kohleveredelung (Kohlevergasung), 1958.

[16] Eckel G, Le Clercq P, Kathrotia T, Saenger A, Fleck S, Mancini M, et al. Entrained flow gasification. part 3: insight into the injector near-field by Large Eddy simulation with detailed chemistry. Fuel 223 2018:164–78. https://doi.org/10.1016/j.fuel.2018.02.176.

[17] Haas M, Dammann M, Fleck S, Kolb T. Entrained flow gasification: Impact of fuel spray distribution on reaction zone structure. Fuel 2023;334:126572. https://doi.org/10.1016/j.fuel.2022.126572.

[18] Mancini M, Alberti M, Dammann M, Santo U, Eckel G, Kolb T, et al. Entrained flow gasification. part 2: mathematical modeling of the gasifier using RANS method. Fuel 225 2018:596–611. https://doi.org/10.1016/j.fuel.2018.03.100.

[19] Dammann M, Santo U, Böning D, Knoch H, Eberhard M, Kolb T. Entrained flow gasification: pilot-scale experimental, balancing and equilibrium data for model validation. Fuel 2025;382(Part A):132809. https://doi.org/10.1016/j.fuel.2024.132809.

[20] Schneider C, Zeller M, Böhm D, Kolb T. Influence of pressure on the gasification kinetics of two high-temperature beech wood chars with CO_2, H_2O and its mixture. Fuel 2021;299:120523. https://doi.org/10.1016/j.fuel.2021.120523.

[21] Schneider C, Walker S, Phounglamcheik A, Umeki K, Kolb T. Effect of calcium dispersion and graphitization during high-temperature pyrolysis of beech wood char on the gasification rate with CO_2. Fuel 2021;283:118826. https://doi.org/10.1016/j.fuel.2020.118826.

[22] Stoesser P, Schneider C, Kreitzberg T, Kneer R, Kolb T. On the influence of different experimental systems on measured heterogeneous gasification kinetics. Appl Energy 2018;211:582–9. https://doi.org/10.1016/j.apenergy.2017.11.037.

[23] Naim W, Springmann L, Fendt S, Spliethoff H. Intrinsic char reactivity and kinetic analysis of biogenic residues in pressurised entrained-flow gasification under industrial-relevant conditions. Fuel 2026;406:136715. https://doi.org/10.1016/j.fuel.2025.136715.

[24] Naim W, Treu P, Dohrn M, Saraçi E, Grunwaldt J-D, Fendt S, et al. Structure-reactivity- and modelling-relationships during thermal annealing in biomass entrained-flow gasification: the effect of temperature and residence time. Fuel 2025;383:133848. https://doi.org/10.1016/j.fuel.2024.133848.

[25] Gonzalez V, Rußig S, Schurz M, Krzack S, Kleeberg J, Guhl S, et al. Experimental investigations on lignite char gasification kinetics using a pressurized drop tube reactor. Fuel 2018;224:348–56. https://doi.org/10.1016/j.fuel.2018.03.018.
[26] Keller F, Küster F, Meyer B. Determination of coal gasification kinetics from integral drop tube furnace experiments with steam and CO2. Fuel 2018;218:425–38. https://doi.org/10.1016/j.fuel.2017.11.120.
[27] Alsaeedi S, Zhang R, Yan B, Wang Z, Li J, Al-Hakeem B, et al. A review of biomass energy and gasification: bibliometrics, hotspots and emerging trends. Biomass Bioenergy 2026;207:108797. https://doi.org/10.1016/j.biombioe.2025.108797.
[28] Comet Technologies Canada Inc., Dragonfly 3D World, 2025.
[29] Gostick J, Aghighi M, Hinebaugh J, Tranter T, Hoeh MA, Day H, et al. OpenPNM: a pore network modeling package. Comput Sci Eng 2016;18:60–74. https://doi.org/10.1109/MCSE.2016.49.
[30] Freisewinkel E, Eisenbach T, Weise V, Tarlinski D, Pörtner L, Cerciello F, et al. Porosity measurement of biomass char by a novel combination of adsorption measurements and an optical method. Int J Energy Clean Environ 2026;27:87–113. https://doi.org/10.1615/InterJEnerCleanEnv.2025056727.
[31] Salatino P, Senneca O, Masi S. Assessment of thermodeactivation during gasification of a bituminous coal char. Energy Fuels 1999;13:1154–9. https://doi.org/10.1021/ef9900334.
[32] Kreitzberg T, Bormann C, Pielsticker S, Hatzfeld O, Kneer R. Thermal deactivation of biogenic and fossil fuels: Experimental investigation and modeling approaches. Energy Procedia 2019;158:2025–30. https://doi.org/10.1016/j.egypro.2019.01.468.
[33] Vázquez-Santos MB, Geissler E, László K, Rouzaud J-N, Martínez-Alonso A, Tascón JM. Comparative XRD, Raman, and TEM study on graphitization of PBO-derived carbon fibers. J Phys Chem C 2012;116:257–68. https://doi.org/10.1021/jp2084499.
[34] Mubari PK, Beguerie T, Monthioux M, Weiss-Hortala E, Nzihou A, Puech P. The X-ray. Raman and TEM Signatures of Cellulose-Derived Carbons Explained, C 2022;8:4. https://doi.org/10.3390/c8010004.
[35] Rhim Y-R, Zhang D, Fairbrother DH, Wepasnick KA, Livi KJ, Bodnar RJ, et al. Changes in electrical and microstructural properties of microcrystalline cellulose as function of carbonization temperature. Carbon 2010;48:1012–24. https://doi.org/10.1016/j.carbon.2009.11.020.
[36] Harris PJF. New perspectives on the structure of graphitic carbons. Crit Rev Solid State Mater Sci 2005;30:235–53. https://doi.org/10.1080/10408430500406265.
[37] Morin M, Pécate S, Hémati M, Kara Y. Pyrolysis of biomass in a batch fluidized bed reactor: effect of the pyrolysis conditions and the nature of the biomass on the physicochemical properties and the reactivity of char. J Anal Appl Pyrol 2016;122:511–23. https://doi.org/10.1016/j.jaap.2016.10.002.
[38] Walker S, Kolb T. Operation of a differential fixed bed reactor for investigations on micro-kinetics of heterogeneous gasification reactions. Fuel 2025;381:133561. https://doi.org/10.1016/j.fuel.2024.133561.
[39] Walker S, Kolb T. Pressurized gasification of beech wood char in steam and steam-CO_2 mixtures: kinetics considering steam-CO_2 interaction. Energy Fuels 2025:acs.energyfuels.5c04287. https://doi.org/10.1021/acs.energyfuels.5c04287.
[40] Wang Y, Bell DA. Competition between H_2O and CO_2 during the gasification of Powder River Basin coal. Fuel 2017;187:94–102. https://doi.org/10.1016/j.fuel.2016.08.109.
[41] Fermoso J, Stevanov C, Moghtaderi B, Arias B, Pevida C, Plaza MG, et al. High-pressure gasification reactivity of biomass chars produced at different temperatures. J Anal Appl Pyrol 2009;85:287–93. https://doi.org/10.1016/j.jaap.2008.09.017.
[42] Zhao S, Ding L, Ruan Y, Bai B, Qiu Z, Li Z. Experimental and kinetic studies on steam gasification of a biomass char. Energies 2021;14:7229. https://doi.org/10.3390/en14217229.
[43] Wedler C, Span R, Richter M. Comparison of micro- and macropore evolution of coal char during pyrolysis. Fuel 2020.
[44] Kwack EY, Shakkottai P, Massier PF, Back LH. Morphology of globules and cenospheres in heavy fuel oil burner experiments. Transactions of the ASME 1992.
[45] Franklin RE. The structure of graphitic carbons. Acta Crys 1951:253–61.
[46] Puech P, Moyano S, Mubari P, Weiss-Hortala E, Monthioux M. Background issues in X-Ray diffraction and Raman spectroscopy of carbon materials. C 2026;12:2. https://doi.org/10.3390/c12010002.
[47] E.K. Gerhard Emig, Chemische Reaktionstechnik, sixth ed., Springer-Verlag GmbH, 2017.
[48] Roberts DG, Harris DJ. A kinetic analysis of coal char gasification reactions at high pressures. Energy Fuels 2006;20:2314–20. https://doi.org/10.1021/ef060270o.
[49] Cetin E, Moghtaderi B, Gupta R, Wall TF. Biomass gasification kinetics: influences of pressure and char structure. Combust Sci Technol 2005;177:765–91. https://doi.org/10.1080/00102200590917266.
[50] Li C, Zhao J, Fang Y, Wang Y. Effect of pressure on gasification reactivity of three Chinese coals with different ranks. Front Chem Eng China 2010;4:385–93. https://doi.org/10.1007/s11705-010-0501-1.
[51] Wedler C, Span R. A pore-structure dependent kinetic adsorption model for consideration in char conversion – adsorption kinetics of CO_2 on biomass chars. Chem Eng Sci 2021;231:116281. https://doi.org/10.1016/j.ces.2020.116281.
[52] Bai Y, Lv P, Yang X, Gao M, Zhu S, Yan L, et al. Gasification of coal char in H_2O/CO_2 atmospheres: evolution of surface morphology and pore structure. Fuel 2018;218:236–46. https://doi.org/10.1016/j.fuel.2017.11.105.
[53] Du Y, Wang C, Xin H, Che D, Mathews JP. Competitive or additive behavior for H_2O and CO_2 gasification of coal char?: exploration via simplistic atomistic simulation. Carbon 2019;141:226–37. https://doi.org/10.1016/j.carbon.2018.09.072.
[54] Stoesser P. Investigation of solid phase processes during the conversion of biogenic slurry in entrained flow gasifiers. Dissertation, Karlsruhe 2019.
[55] Buffham BA. Design relations for hollow catalyst pellets. Chem Eng Res Des 2000;78:269–82. https://doi.org/10.1205/026387600527130.
[56] Rossberg M, Wicke E. Transportvorgänge und Oberflächenreaktionen bei der Verbrennung graphitischen Kohlenstoffs. Chemie Ingenieur Technik 1956;28:181–9. https://doi.org/10.1002/cite.330280309.